Dynamic regulation and requirement for ribosomal RNA transcription during mammalian development

Karla T. Falcon[a,1], Kristin E. N. Watt[a,1,2], Soma Dash[a,1,2], Ruonan Zhao[a,b], Daisuke Sakai[a,c], Emma L. Moore[a], Sharien Fitriasari[a], Melissa Childers[a], Mihaela E. Sardiu[a,d], Selene Swanson[a], Dai Tsuchiya[a], Jay Unruh[a], George Bugarinovic[a,e], Lin Li[f], Rita Shiang[f], Annita Achilleos[a,g], Jill Dixon[h], Michael J. Dixon[h], and Paul A. Trainor[a,b,2]

Ribosomal RNA (rRNA) transcription by RNA polymerase I (Pol I) is a critical rate-limiting step in ribosome biogenesis, which is essential for cell survival. Despite its global function, disruptions in ribosome biogenesis cause tissue-specific birth defects called ribosomopathies, which frequently affect craniofacial development. Here, we describe a cellular and molecular mechanism underlying the susceptibility of craniofacial development to disruptions in Pol I transcription. We show that Pol I subunits are highly expressed in the neuroepithelium and neural crest cells (NCCs), which generate most of the craniofacial skeleton. High expression of Pol I subunits sustains elevated rRNA transcription in NCC progenitors, which supports their high tissue-specific levels of protein translation, but also makes NCCs particularly sensitive to rRNA synthesis defects. Consistent with this model, NCC-specific deletion of Pol I subunits *Polr1a*, *Polr1c*, and associated factor *Tcof1* in mice cell-autonomously diminishes rRNA synthesis, which leads to p53 protein accumulation, resulting in NCC apoptosis and craniofacial anomalies. Furthermore, compound mutations in Pol I subunits and associated factors specifically exacerbate the craniofacial anomalies characteristic of the ribosomopathies Treacher Collins syndrome and Acrofacial Dysostosis–Cincinnati type. Mechanistically, we demonstrate that diminished rRNA synthesis causes an imbalance between rRNA and ribosomal proteins. This leads to increased binding of ribosomal proteins Rpl5 and Rpl11 to Mdm2 and concomitantly diminished binding between Mdm2 and p53. Altogether, our results demonstrate a dynamic spatiotemporal requirement for rRNA transcription during mammalian cranial NCC development and corresponding tissue-specific threshold sensitivities to disruptions in rRNA transcription in the pathogenesis of congenital craniofacial disorders.

RNA polymerase 1 | neural crest cells | rRNA transcription | ribosome biogenesis | Mdm2-p53

Ribosomal RNA (rRNA) transcription and ribosome biogenesis are critical for cell growth, proliferation, differentiation, and survival. Ribosomes translate cellular proteins and are responsible for the quality and quantity of proteins (1, 2). The ability to modulate translation rates and translation capacity to meet cell-specific needs is regulated in part by the number of ribosomes available to translate messenger RNAs (mRNAs) (2–5). A critical rate-limiting step in ribosome biogenesis is RNA polymerase (Pol) I–mediated rRNA transcription (6, 7), which accounts for about 60% of all cellular transcription (2, 8) and is integral to increased protein translation during cell growth and proliferation and in response to other metabolic needs. In mammals, Pol I consists of 10 core, 1 stalk, and 2 dissociable subunits (9) that transcribe the 47S precursor rRNA, which is then modified, processed, and cleaved into 5.8S, 18S, and 28S rRNAs. These rRNAs, together with 5S rRNAs transcribed by Pol III, associate with ribosomal proteins and form the catalytic core of the ribosome (10).

Considering the requirement for Pol I-mediated rRNA transcription and ribosome biogenesis in all cell types, it is surprising that defects in these processes result in cancers or tissue-specific developmental disorders known as ribosomopathies (11–14). For example, mutations in the Pol I catalytic subunit *POLR1A* result in Acrofacial Dysostosis–Cincinnati type (AFDCIN) (15), whereas mutations in *POLR1C* and *POLR1D*, shared subunits of Pol I and III, or Pol I-associated factor *TCOF1* cause Treacher Collins syndrome (TCS) (16–18). *TCOF1* encodes the nucleolar phosphoprotein TREACLE, which is involved in rRNA transcription and processing, as well as in DNA damage repair (19–21). AFDCIN and TCS present with a range of phenotypes, which primarily include abnormal craniofacial skeletal development, micrognathia, cleft palate, and malar hypoplasia (15, 17, 18). The majority of the craniofacial tissues affected in TCS and AFDCIN are derived from neural crest cells (NCCs). NCCs are a transient progenitor population, which arise from the neuroepithelium and then delaminate, proliferate, and migrate into

Significance

RNA polymerase I (Pol I)–mediated ribosomal RNA (rRNA) transcription is required for protein synthesis in all cells for normal growth and survival, as well as for proper embryonic development. Interestingly, disruptions in Pol I-mediated transcription perturb ribosome biogenesis and lead to tissue-specific birth defects, which commonly affect the head and face. Our results show that during mouse development, Pol I-mediated rRNA transcription and protein translation are tissue specifically elevated in neural crest cells, which give rise to bone, cartilage, and ganglia in the head and face. Using mouse models, we further show that neural crest cells are highly sensitive to disruptions in Pol I and that when rRNA synthesis is genetically down-regulated, it results in craniofacial anomalies.

the frontonasal prominences and pharyngeal arches, where they differentiate into most of the craniofacial bone and cartilage, among other tissues (22). TCS and AFDCIN are therefore considered both ribosomopathies and neurocristopathies due to deficits in ribosome biogenesis and NCC development. Previous work has elucidated the basic functions of proteins involved in rRNA transcription and ribosome biogenesis in various organisms, including yeast and human cell lines (23–25), and demonstrated that mutations in *Tcof1*, *polr1a*, *polr1c*, and *polr1d* disrupt NCC development (15, 26–29). However, the mechanisms by which global disruptions in Pol I–mediated transcription result in tissue-specific phenotypes remain poorly understood. In particular, it has not yet been determined 1) why cranioskeletal development is highly susceptible to defects in rRNA transcription and 2) if rRNA transcription is tissue-specifically required during mammalian craniofacial development.

We hypothesized that different cells and tissues have distinct threshold requirements for rRNA transcription, ribosome biogenesis, and protein synthesis to meet their cell-specific needs and that this leads to distinct cell- and tissue-specific threshold sensitivities to deficiencies in rRNA transcription. Given the high incidence of cranioskeletal defects in ribosomopathies, we posited that NCCs are one of the cell types that require high levels of rRNA and protein synthesis. We therefore examined the role of Pol I and rRNA transcription in NCCs during craniofacial development. Through lineage tracing, expression, and translation analyses, we discovered that neuroepithelial cells and NCCs exhibit elevated levels of rRNA transcription that correlate with high levels of protein translation compared with surrounding cells during early embryogenesis.

To understand the intrinsic function of Pol I-mediated transcription in NCCs, we generated models of Pol I disruption via null and conditional tissue-specific deletion of a catalytic subunit (*Polr1a*), noncatalytic subunits (*Polr1c* and *Polr1d*), and associated factor (*Tcof1*) of Pol I in mice. We discovered that Pol I-mediated transcription is essential for cell survival and that cranial NCCs are particularly sensitive to decreased rRNA transcription during early craniofacial development. Pol I subunit and associated factor loss-of-function results in rRNA deficiency, which perturbs the stoichiometric balance between rRNA and ribosomal proteins. This imbalance leads to ribosomal stress and increased binding of ribosomal proteins RPL5 (uL18) and RPL11 (uL5) to Murine double minute 2 (Mdm2), a major regulator of p53 activity. Concomitantly, Mdm2 binding to p53 is reduced, which results in p53 accumulation in the nucleus and, consequently, NCC apoptosis and craniofacial anomalies. Thus, global perturbation of rRNA transcription leads to tissue-specific posttranslational accumulation of p53 protein, which contributes to the tissue specificity of developmental ribosomopathy phenotypes. Taken together, our work demonstrates the dynamic tissue-specific regulation and requirement for rRNA transcription during craniofacial development that mechanistically accounts for tissue-specific threshold sensitivities to perturbation of rRNA transcription. Finally, our data show that ubiquitously expressed genes thought to play fundamental housekeeping functions exhibit cell-type-specific functions, providing insights into the roles of rRNA transcription in regulating embryonic development and disease.

Results

Cranial NCCs Have High Levels of rRNA and Protein Synthesis. Mutations in Pol I subunits result in tissue-specific craniofacial anomalies in humans (15, 16, 30). We hypothesized that the underlying cause for these tissue-specific defects is differential transcription of rRNA in NCCs during early embryogenesis. We therefore performed ViewRNA in situ hybridization (31) for the 47S preribosomal RNA (prerRNA) 5′ External Transcribed Spacer (ETS) (Fig. 1*A*) as a measure of nascent rRNA transcription (32, 33) in *Wnt1-Cre;ROSAeYFP* mouse embryos. This transgenic combination lineage labels the dorsal neuroepithelium, including NCC progenitors and their descendants, with yellow fluorescent protein (YFP) (34). At embryonic day (E) 8.5, during NCC formation and early migration, 5′ETS was globally expressed. However, 5′ETS expression was significantly higher in NCCs (YFP+ cells) relative to surrounding non-NCCs (YFP− cells) (Fig. 1 *B* and *C*). At E9.5, during later migration and the onset of differentiation, 5′ETS expression remained higher in NCCs versus non-NCCs (Fig. 1 *D* and *E*), although quantitatively, the difference was less than observed at E8.5. This indicates that NCC have endogenously high levels of rRNA transcription at early stages of development while they are in a more progenitor and highly proliferative state compared with surrounding tissues.

Given its importance as a rate-limiting step in ribosome biogenesis, which leads to translation of all cellular protein, we hypothesized that high rRNA transcription in NCCs would correlate with elevated protein synthesis. To test this idea, we performed *O*-propargyl-puromycin (OPP) labeling as a measure of nascent translation (35) in *Wnt1-Cre;ROSAeYFP* embryos, which revealed that cranial NCCs have significantly higher protein synthesis compared with other surrounding cells at E8.5 (Fig. 1 *F* and *G*) and slightly higher, although not statistically significant, levels of protein synthesis at E9.5 (Fig. 1 *H* and *I*). To determine whether increased ribosomal DNA (rDNA) transcription and translation correlates with tissue-specific proliferative capacity, we performed 5-bromo-2′-deoxyuridine (BrdU) incorporation in E8.5 wild-type embryos and immunostained transverse sections for BrdU and the mitotic marker phospho-Histone H3 (pHH3). We observed that the neuroepithelium, which includes premigratory NCCs, is more proliferative than the surrounding mesoderm and endoderm (*SI Appendix*, Fig. S1 *A* and *B*). Together, these observations reveal a correlation between high proliferation with elevated rRNA transcription and protein synthesis at E8.5 in neuroepithelial cells and NCC progenitors. Consequently, we posited that the neuroepithelium and NCCs would be particularly sensitive to disruptions in Pol I–mediated rRNA transcription during embryonic development. Indeed, culturing E8.5 wild-type mouse embryos for as short as 8 h with a Pol I inhibitor, BMH-21 (36), resulted in apoptosis specifically in neuroepithelial cells and NCC progenitors (Fig. 1 *J–L* and *SI Appendix*, Fig. S2). Our data therefore demonstrate that endogenously high rRNA transcription and protein translation in the neuroepithelium and NCC progenitors underpins their cell survival-specific threshold sensitivity to disruptions in Pol I.

Polr1a, _Polr1c_, _Polr1d_, and _Tcof1_ Are Broadly Expressed with Elevated Levels in the Neuroepithelium and Pharyngeal Arches. To understand if tissue-specific differences in rRNA transcription correlate with differential expression of Pol I subunits during embryogenesis, we examined the expression of *Polr1a*, *Polr1c*, *Polr1d*, and the associated factor Treacle, which is encoded by *Tcof1*, during early embryogenesis. *Polr1a*$^{+/-}$, *Polr1c*$^{+/-}$, and *Polr1d*$^{+/-}$ mice carrying a gene trap vector with a βGeo cassette in the endogenous locus of each gene were generated (*SI Appendix*, Fig. S3*A*), allowing for evaluation of *Polr1a*, *Polr1c*, and *Polr1d* spatiotemporal gene expression by LacZ
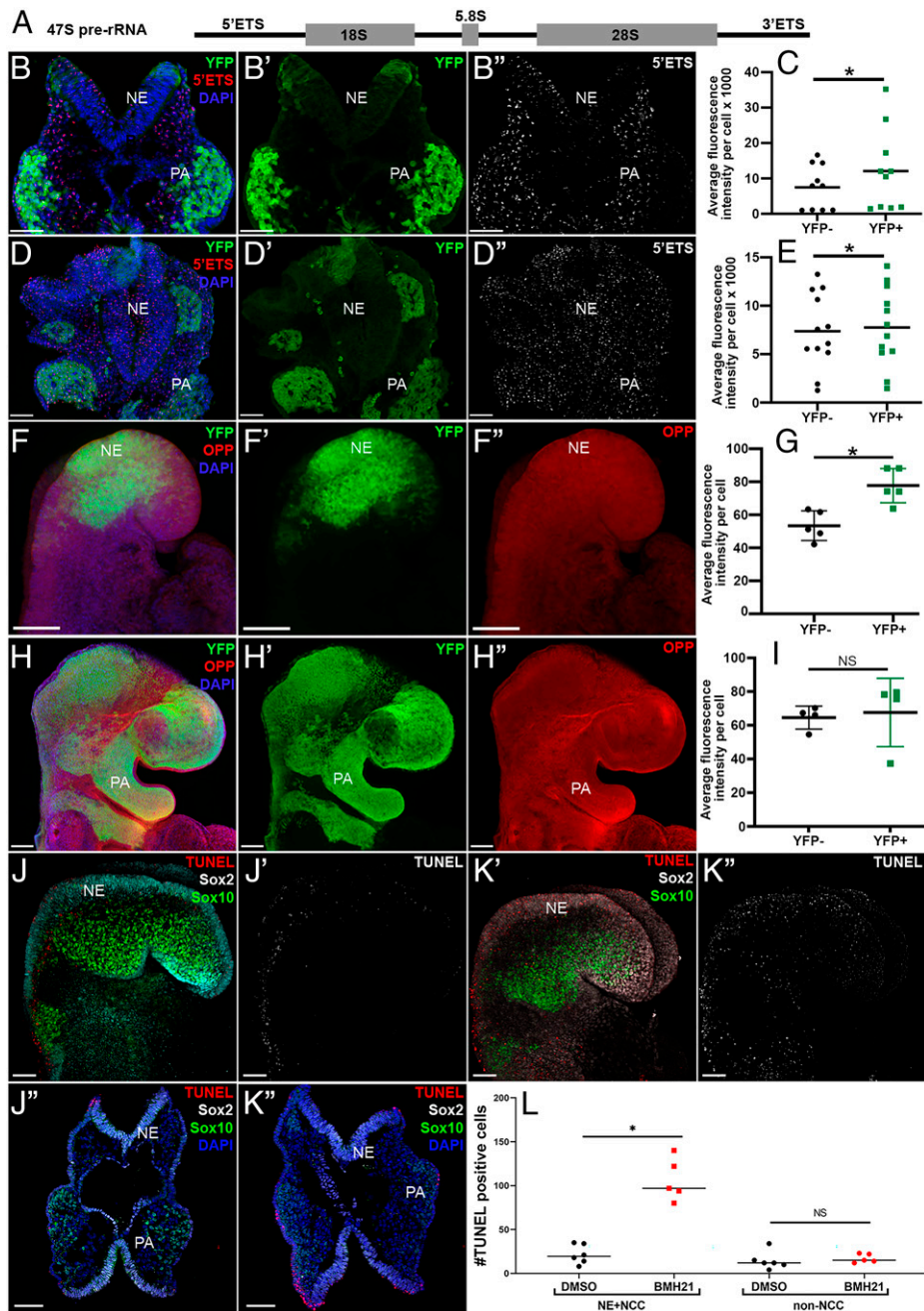
Fig. 1. Elevated levels of rRNA synthesis in NCCs results in high sensitivity to disruptions in Pol I. (*A*) Diagram of 47S prerRNA showing the 5′ETS, 18S, 5.8S, and 28S rRNA components and 3′ETS. (*B–E*) Fluorescence in situ hybridization using ViewRNA for the 5′ETS of the 47S prerRNA in transverse sections of wild-type *Wnt1-Cre;ROSAeYFP* embryos. At E8.5, 5′ETS expression (red in *B*, white in *B″*) is significantly higher in NCCs (YFP+; *B′*) compared with non-NCCs (YFP−); quantification is in *C*. At E9.5, 5′ETS expression (*D* and *D″*) remains slightly higher in NCCs (*D′*) compared with non-NCCs (*D″*); quantification is in *E*. (*F–I*) Nascent protein synthesis was analyzed via OPP incorporation in wild-type *Wnt1-Cre; ROSAeYFP* embryos. (*F*) NCCs (YFP+) have elevated OPP staining at E8.5 relative to non-NCCs (YFP−); quantification is in *G*. (*H*) OPP staining is comparable between NCCs and non-NCCs by E9.5; quantification is in *I*. (*J* and *K*) Disruption of Pol I transcription in wild-type embryos at E8.5 with Pol I inhibitor BMH-21 (*K*, *K′*, and *K″*) results in increased TUNEL-positive cells (red in *J*, *J″*, *K*, and *K″* and white in *J′* and *K′*) in the neuroepithelium (labeled with Sox2), including the dorsal neuroepithelium, where NCC progenitors (labeled with Sox10) are located compared with DMSO-treated embryos (*J*, *J′*, and *J″*). Transverse sections confirm increased TUNEL staining in BMH-21–treated embryos (*K″*) relative to controls (*J″*). (*L*) Quantification of TUNEL-positive cells in DMSO-treated and BMH-21–treated embryos in NCCs and non-NCCs. *P < 0.05 using the paired *t* test. NE, neuroepithelium; NS, not significant; PA, pharyngeal arches. (Scale bars, 100 μm).

staining. *Polr1a*, *Polr1c*, and *Polr1d* were broadly expressed at E8.5 (Fig. 2 *A–C*) and E9.5 (Fig. 2 *I–K*), although *Polr1d* expression was more restricted at this later stage, with high levels of expression in the neuroepithelium and pharyngeal arches, which are the bilateral structures that develop into the jaw and neck (Fig. 2 *E–G* and *M–O*). Similarly, Treacle immunostaining of wild-type embryos revealed broad expression in E8.5 and E9.5 embryos, with elevated levels in the neuroepithelium and pharyngeal arches (Fig. 2 *D*, *H*, *L*, and *P*). Furthermore, single-cell RNA sequencing of E8.5 embryos revealed that all the Pol I subunits, including *Polr1a*, *Polr1c*, and *Polr1d*, as well as *Tcof1*, were expressed broadly in progenitor craniofacial cells and tissues (*SI Appendix*, Fig. S4), but each exhibited enriched expression in the neuroepithelium and NCCs. Altogether, this suggests that elevated expression of Pol I subunits and associated factor *Tcof1* in the neuroepithelium and NCCs contributes to their high levels of rRNA transcription.

To determine the function of individual Pol I subunits during development, heterozygous and homozygous *Polr1a*, *Polr1c*, and *Polr1d* mutant mice were generated (*SI Appendix*, Fig. S3). *Polr1a*$^{+/-}$, *Polr1c*$^{+/-}$, and *Polr1d*$^{+/-}$ embryos were morphologically indistinguishable from their wild-type littermates at E18.5 and survived to adulthood, indicating that a single copy of each gene is sufficient for proper development in mice (*SI Appendix*, Fig. S3B). However, *Polr1a*$^{-/-}$ (n = 23), *Polr1c*$^{-/-}$ (n = 22), and *Polr1d*$^{-/-}$ (n = 20) embryos were embryonic lethal by E3.5 (*SI Appendix*, Fig. S3C). Their arrest at the morula stage and failure to develop into blastocysts and implant demonstrate that these genes are necessary for survival during preimplantation mammalian development.

Polr1a, *Polr1c*, and *Polr1d* Genetically Interact with *Tcof1* during Craniofacial Development. Given their largely overlapping expression patterns with elevated levels in the neuroepithelium
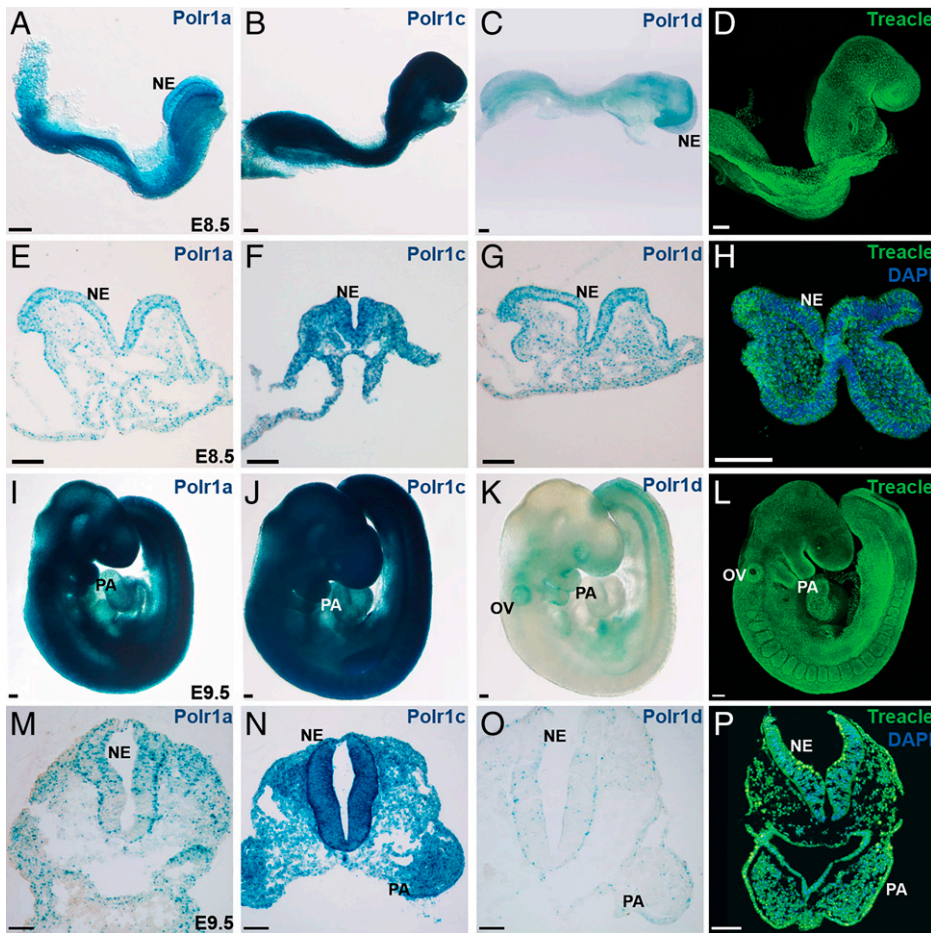
Fig. 2. Pol I subunits and associated factor Treacle are broadly expressed during mouse embryogenesis. (*A–C*) Broad expression of Pol I subunits *Polr1a*, *Polr1c*, and *Polr1d*, as observed by LacZ staining in E8.5 embryos. (*E–G*) Transverse sections through the cranial region indicate high levels of *Polr1a* (*E*), *Polr1c* (*F*), and *Polr1d* (*G*) expression in the neuroepithelium. (*I–K*) At E9.5, *Polr1a* and *Polr1c* remain broadly expressed (*I* and *J*), while *Polr1d* is expressed specifically in the neuroepithelium, pharyngeal arches, otic vesicle, and somites (*K*). Transverse sections through the cranial region at E9.5 indicate higher expression of *Polr1a* (*M*), *Polr1c* (*N*), and *Polr1d* (*O*) in the neuroepithelium and pharyngeal arches compared with surrounding tissues. (*D*, *H*, *L*, and *P*) Immunostaining for Treacle reveals broad expression in whole-embryo and transverse sections of E8.5 and E9.5 embryos, with dynamic elevated levels in the neuroepithelium (*H* and *P*). NE, neuroepithelium; OV, otic vesicle; PA, pharyngeal arches. (Scale bars, 100 μm).

and NCCs, together with their shared Pol I-associated function in rRNA transcription, we hypothesized that *Polr1a*, *Polr1c*, and *Polr1d* genetically interact with *Tcof1* during mouse craniofacial development. In support of this idea, we performed Multi-Dimensional Protein Identification Technology (MudPIT) analysis (37, 38) of HEK293T-derived cell lines stably expressing FLAG-tagged mouse Treacle and found that Treacle pulled down human Pol I subunits, including POLR1A and POLR1C, together with previously known direct targets, such as Casein kinase II subunits (Fig. 3*A* and *SI Appendix*, Fig. S5 and Table S1) (39). Thus, POLR1A, POLR1C, and TREACLE interact at a protein level either directly or possibly through a protein–RNA intermediate consistent with being components and associated factors of Pol I.

To functionally test whether these factors interact at a genetic level, we generated *Tcof1*+/−;*Polr1a*+/−, *Tcof1*+/−;*Polr1c*+/−, and *Tcof1*+/−;*Polr1d*+/− double heterozygous mutants. As described (26, 40), and compared with controls (Fig. 3 *C* and *H*), E18.5 *Tcof1*+/− mouse embryos displayed craniofacial malformations, including dome-shaped heads and hypoplasia of the skull, nasal, premaxillary and maxillary bones, together with partially penetrant cleft palate and ear and eye abnormalities (Fig. 3 *B*, *D*, and *I* and *SI Appendix*, Fig. S6 *A* and *B*), which phenocopies TCS in humans. By comparison, each of the E18.5 double heterozygote mutants exhibited craniofacial defects considerably more severe than found in *Tcof1*+/− embryos (Fig. 3 *B* and *D–G*). Double heterozygotes display exacerbated craniofacial malformations, including fully penetrant cleft palate, together with exencephaly and microphthalmia (Fig. 3 *B* and *D–L*). Furthermore, Alcian blue and Alizarin red staining revealed the comparatively

more severe hypoplasia and malformation of craniofacial cartilage and bone, particularly of the skull, maxilla, and mandible (Fig. 3 *I–L* and *SI Appendix*, Fig. S6 *K–W*), illustrating the particular sensitivity of craniofacial tissues to perturbations in Pol I function.

Interestingly, the double heterozygous mutant embryos also exhibited variably penetrant developmental anomalies outside of the craniofacial region, which were not observed in *Tcof1*+/− embryos. These included thoracoschisis or omphalocele (fissure of the thoracic or abdominal wall) (Fig. 3*B* and *SI Appendix*, Fig. S6 *A–E*), as well as limb and digit anomalies, such as long-bone hypoplasia and an abnormal number or short and broad digits (*SI Appendix*, Fig. S6 *F–J*). While the penetrance of these phenotypes was slightly variable across the double heterozygous mice, we hypothesize that the maternal environment, as well as the background of the *Tcof1* mouse strain, contributes to some of the phenotypic variability (41). Nonetheless, the exacerbated and complete penetrance of cranioskeletal malformations compared with partial penetrance of other tissue anomalies demonstrates the different threshold sensitivities of distinct tissues to global disruptions in Pol I function. These protein and genetic interactions and the additive effects of their loss-of-function reiterate the importance of tissue-specific levels of rRNA transcription and illustrate that *Polr1a*, *Polr1c*, *Polr1d*, and *Tcof1* function together in rRNA transcription in mammalian NCCs during craniofacial development.

NCC-Specific Deletion of *Polr1a*, *Polr1c*, and *Tcof1* Results in Craniofacial Defects. Elevated rRNA transcription in NCC progenitors and NCCs and the high sensitivity of neuroepithelial and craniofacial tissues to defects in rRNA transcription
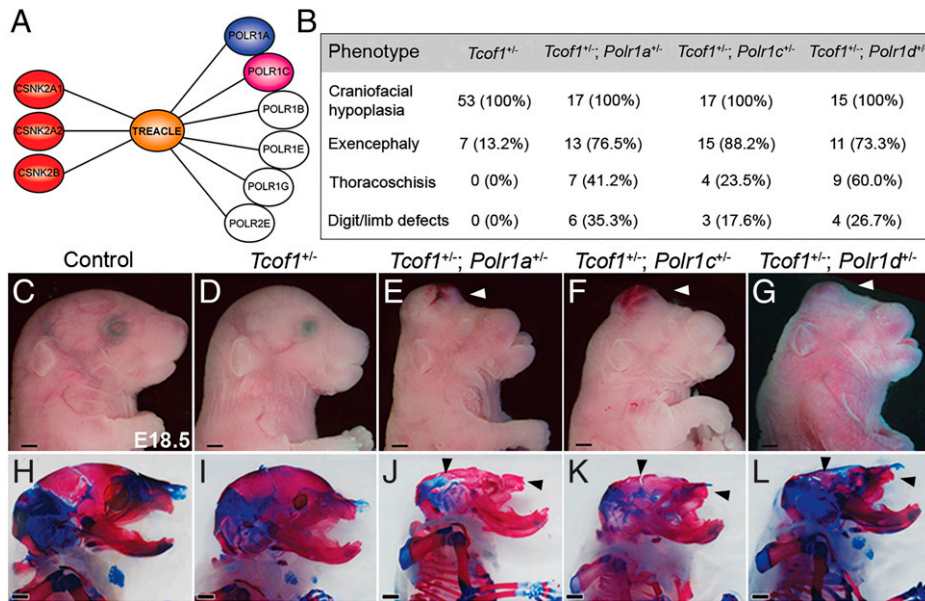
Fig. 3. *Tcof1* and Pol I subunits genetically interact, affecting craniofacial development. (*A*) MudPIT analysis for Treacle-binding proteins recognizes known binding proteins, such as Casein kinase II proteins, as well as Pol I protein subunits, including POLR1A and POLR1C. (*B*) $Tcof1^{+/-}$, $Tcof1^{+/-};Polr1a^{+/-}$, $Tcof1^{+/-};Polr1c^{+/-}$, and $Tcof1^{+/-};Polr1d^{+/-}$ double mutants present with developmental defects with variable penetrance. Table indicates the number of embryos observed with a phenotype. The percentages of the total number of mutants observed are indicated in parentheses. (*C–G*) Brightfield images of $Tcof1^{+/-};Polr1a^{+/-}$, $Tcof1^{+/-};Polr1c^{+/-}$, and $Tcof1^{+/-};Polr1d^{+/-}$ embryos indicate that these double heterozygous mutants exhibit more severe craniofacial defects compared with $Tcof1^{+/-}$ mutants alone, including exencephaly (white arrowheads). (*H–L*) Alizarin red and Alcian blue staining for bone and cartilage, respectively, reveals hypoplastic cartilage and/or bone and craniofacial anomalies, including smaller maxilla and flattened skulls (black arrowheads) in double-mutant embryos (*J–L*) compared with $Tcof1^{+/-}$ mutants (*I*) alone. (Scale bars, 500 μm).

suggest a cell-autonomous role for *Polr1a*, *Polr1c*, and *Tcof1* in Pol I transcription in NCCs during early development. We therefore conditionally deleted these factors in NCCs during their formation using *Wnt1-Cre* transgenic mice. *Wnt1-Cre* recombinase is expressed in the dorsal neuroepithelium, which includes NCC progenitors beginning at E8.5 (34, 42). We crossed *Wnt1-Cre* mice with $Polr1a^{flx/flx}$, $Polr1c^{flx/flx}$, or $Tcof1^{flx/flx}$ mice to generate NCC-specific knockouts (NKOs) of *Polr1a*, *Polr1c*, and *Tcof1* (*SI Appendix*, Fig. S7*A*). The levels of *Polr1a*, *Polr1c*, and *Tcof1* transcripts in NCCs were reduced in E9.5 $Polr1a^{NKO/NKO}$, $Polr1c^{NKO/NKO}$, and $Tcof1^{NKO/NKO}$ mutant embryos, respectively, relative to littermate $Polr1a^{NKO/+}$, $Polr1c^{NKO/+}$, and $Tcof1^{NKO/+}$ controls, confirming Cre-mediated excision of exons flanked by loxP sites (*SI Appendix*, Fig. S7*B*).

E9.5 $Polr1a^{NKO/NKO}$, $Polr1c^{NKO/NKO}$, and $Tcof1^{NKO/NKO}$ mutants presented with visibly hypoplastic frontonasal prominences and pharyngeal arches when compared with littermate controls, a phenotype that worsened considerably by E10.5 to E11.5 (Fig. 4 *A–D* and *SI Appendix*, Fig. S8 *A–H*). To determine whether this tissue hypoplasia was a consequence of perturbed NCC development, we crossed *ROSAeYFP* into the background of $Polr1a^{NKO/NKO}$, $Polr1c^{NKO/NKO}$, and $Tcof1^{NKO/NKO}$ mice to indelibly label the NCC lineage with YFP (43). This revealed that NCCs migrate into the facial prominences and pharyngeal arches in *NKO* mutants by E9.5 (*SI Appendix*, Fig. S8 *I–L*). However, the smaller facial outgrowths in these mutants appeared to correlate with reduced populations of NCCs, a phenotype that was even more pronounced at E10.5 in the *NKO* mutants compared with littermate controls (Fig. 4 *E–H* and *Q–T*). $Polr1a^{NKO/NKO}$ embryos had the most severe reduction in the NCC population, consistent with its essential role as part of the catalytic core of Pol I. The NCC population was also severely hypoplastic in $Polr1c^{NKO/NKO}$ and $Tcof1^{NKO/NKO}$ embryos, although to a slightly lesser degree than $Polr1a^{NKO/NKO}$ embryos. Reflecting this difference in severity, $Polr1a^{NKO/NKO}$ embryos died around E11.5, whereas $Polr1c^{NKO/NKO}$ and $Tcof1^{NKO/NKO}$ embryos survived until E12.5 and E13.5, respectively (*SI Appendix*, Fig. S7 *C* and *D*), conveying the relative importance of *Polr1a*, *Polr1c*, and *Tcof1* in NCCs for embryo survival.

NCCs differentiate into a wide variety of cell and tissue derivatives, including neurons in the peripheral nervous system

and osteochondroprogenitors of craniofacial cartilage and bone. To examine NCC differentiation into neurons, we stained for neuron-specific class III β-tubulin (TuJ1) at E10.5. This revealed that $Polr1a^{NKO/NKO}$ and $Polr1c^{NKO/NKO}$ mutants exhibit hypoplastic cranial ganglia, especially the trigeminal (V), together with diminished nerve projections compared with littermate controls (Fig. 4 *I–K*). The trigeminal in $Tcof1^{NKO/NKO}$ mutants displayed altered morphology and smaller nerve projections, consistent with a reduced population of NCCs (Fig. 4*L*). The early lethality of *NKO* mutant embryos prevented analysis of NCC differentiation into mature cartilage and bone. Therefore, we investigated the specification of NCCs into osteochondroprogenitors. The expression of Sox9, a master regulator of chondrogenesis, and its downstream target, *Col2a1* (44), were both diminished in the facial prominences in E9.5 and E10.5 *NKO* mutants compared with controls (Fig. 4 *M–P* and *SI Appendix*, Fig. S8 *M–P* and *Q–T*). The reduced domains of chondrogenic gene expression, especially the first and second pharyngeal arches, and hypoplastic cranial ganglia likely reflect the reduced number of NCCs within the arches in *NKO* mutants (Fig. 4 *E–H* and *SI Appendix*, Fig. S8 *I–L*). Furthermore, smaller craniofacial prominences and pharyngeal arches (Fig. 4 *A–D* and *Q–T*) suggest that *Polr1a*, *Polr1c*, and *Tcof1* play critical roles in NCC proliferation and/or survival.

***Polr1a*, *Polr1c*, and *Tcof1* Loss-of-Function in NCCs Leads to Increased NCC Death.** We hypothesized that decreased proliferation and/or increased apoptosis accounts for the reduced NCC population in *NKO* mutants. Transverse sections of E9.5 $Polr1a^{NKO/NKO};ROSAeYFP$, $Polr1c^{NKO/NKO};ROSAeYFP$, and $Tcof1^{NKO/NKO};ROSAeYFP$ embryos were stained for the mitotic proliferation marker pHH3. Quantification revealed that while mutant embryos displayed slightly fewer pHH3+ NCCs compared with littermate controls, the differences were not statistically significant at this stage (Fig. 5 *A–D* and *SI Appendix*, Fig. S9*A*). In contrast, $Polr1a^{NKO/NKO};ROSAeYFP$, $Polr1c^{NKO/NKO};ROSAeYFP$, and $Tcof1^{NKO/NKO};ROSAeYFP$ mutant embryos exhibit increased terminal deoxynucleotidyl transferase dUTP nick-end labeling (TUNEL) staining of NCCs (Fig. 5 *E–H* and *SI Appendix*, Fig. S9*B*), especially within the pharyngeal arches (Fig. 5 *E–H*).
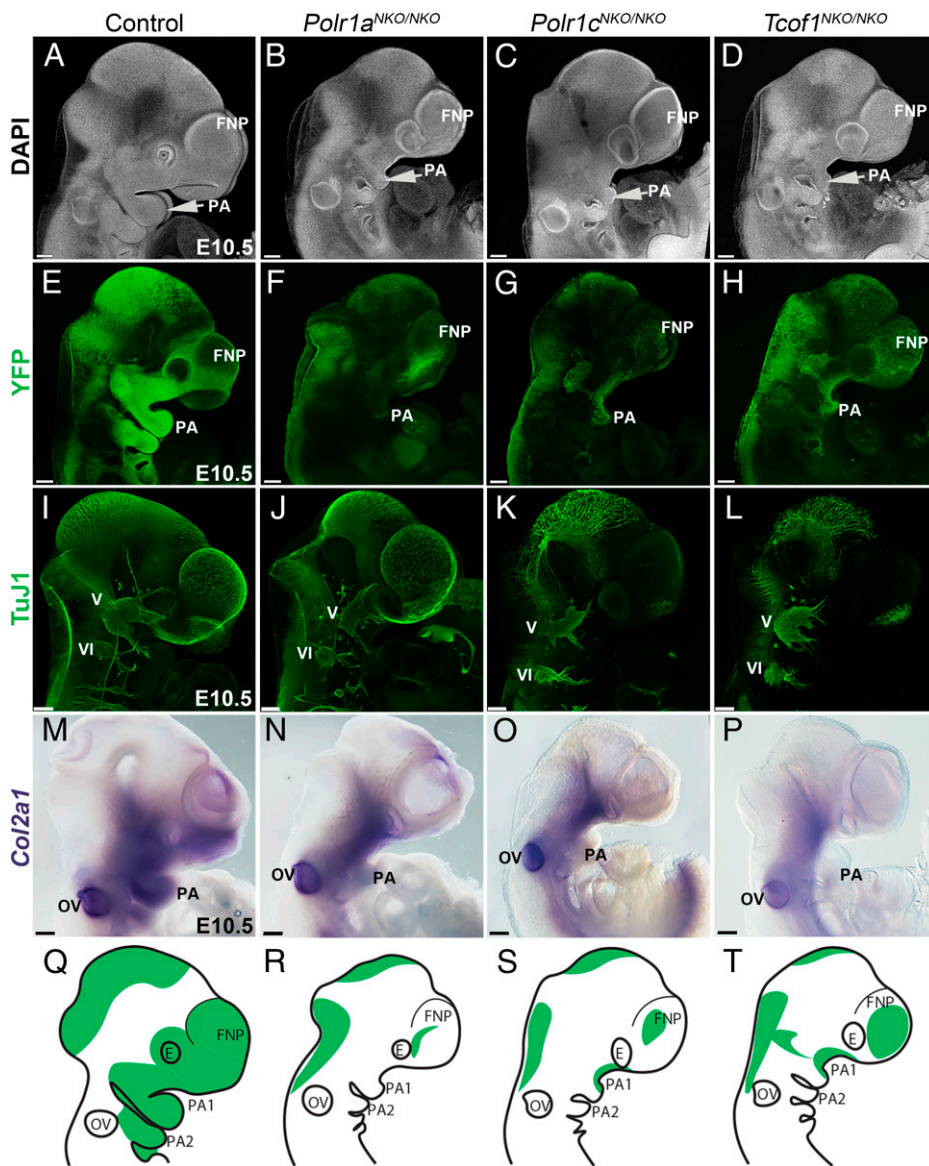
Fig. 4. *Polr1a*, *Polr1c*, and *Tcof1* are required for NCCs and craniofacial development in mice. (*A–D*) DAPI staining at E10.5 shows hypoplastic pharyngeal arches (white arrow) and frontonasal prominences in *Polr1a*$^{NKO/NKO}$, *Polr1c*$^{NKO/NKO}$, and *Tcof1*$^{NKO/NKO}$ embryos compared with control embryos. (*E–H*) *Polr1a*$^{NKO/NKO}$, *Polr1c*$^{NKO/NKO}$, and *Tcof1*$^{NKO/NKO}$ were bred into the background of *ROSAeYFP* mice to label the NCC lineage with YFP. YFP staining indicates fewer NCCs in the pharyngeal arches and frontonasal prominences in *Polr1a*$^{NKO/NKO}$, *Polr1c*$^{NKO/NKO}$, and *Tcof1*$^{NKO/NKO}$ embryos. (*I–L*) Neuron-specific class III β-tubulin (TuJ1) staining indicates that NCC differentiation to neurons and glia is disrupted in *Polr1a*$^{NKO/NKO}$, *Polr1c*$^{NKO/NKO}$, and *Tcof1*$^{NKO/NKO}$ embryos. The trigeminal (V) nerve ganglia are hypoplastic in all mutants. (*M–P*) In situ hybridization for chondrogenesis marker *Col2a1* shows reduced expression, especially within the pharyngeal arches in *Polr1a*$^{NKO/NKO}$, *Polr1c*$^{NKO/NKO}$, and *Tcof1*$^{NKO/NKO}$ embryos. (*Q–T*) Schematic figures depicting hypoplastic pharyngeal arches and frontonasal prominences as well as decreased NCCs (green) in mutants versus controls. FNP, frontonasal prominence; OV, otic vesicle; PA, pharyngeal arches. (Scale bars, 200 µm).

p53 is a well-known mediator of apoptosis (45), and its mRNA level (46) or protein activity (27, 47) have each been proposed to underlie tissue-specific defects in the neuroepithelium. We therefore quantified *p53* expression by qPCR and found no significant changes in *p53* transcription between NCCs and non-NCCs in wild-type embryos (*SI Appendix*, Fig. S10A), but *p53* was slightly reduced in the NCCs of *Polr1a*$^{NKO/NKO}$ mutants compared with *Polr1a*$^{NKO/+}$ controls (*SI Appendix*, Fig. S10A). This demonstrates that differences in *p53* mRNA levels do not underlie differences in cell death, consistent with our previous studies (26, 27). Interestingly, p53 protein is uniformly expressed across different tissues at very low levels in wild-type E8.5 embryos (27), and although *p53* was not affected at the transcript level, p53 protein was tissue-specifically increased in the neuroepithelium and pharyngeal arches in *NKO* mutants compared with their respective littermate controls (Fig. 5 *I–L* and *SI Appendix*, Fig. S9C). While p53 protein levels were not significantly increased in *Polr1a*$^{NKO/NKO}$ mice at this stage, examination of cell-cycle inhibitor and p53 target gene *p21* by qPCR demonstrated a significant increase in the NCCs of *Polr1a*$^{NKO/NKO}$ mutants (*SI Appendix*, Fig. S10A). This suggests that there may be an effect on proliferation downstream of p53 activation and that the difference in pHH3 observed (Fig. 5 *A* and *B*), while not statistically significant, may be biologically significant to the mutant phenotype. To confirm that the up-regulation of p53 is biologically relevant in the *Polr1a*$^{NKO/NKO}$ mutant mice, we treated these embryos and littermate controls with a p53 inhibitor, pifithrin-α (48). *Polr1a*$^{NKO/NKO}$ mice treated with pifithrin-α showed a considerable increase in the volume of the pharyngeal arches in concert with increased YFP+ cells in the arches and frontonasal prominences (*n* = 3/4) compared with *Polr1a*$^{NKO/NKO}$ mutants treated with dimethyl sulfoxide (DMSO) (*SI Appendix*, Fig. S10B). This indicates that increased p53-dependent cell death reduces the NCC population in *Polr1a*$^{NKO/NKO}$ mutants. However, these pifithrin-α treated *Polr1a*$^{NKO/NKO}$ embryos do not survive beyond E12.5, probably because inhibiting p53 does not rescue rRNA synthesis and ribosomal stress. Altogether, our results signify that the NCC population in *NKO* mutants is diminished primarily due to a cell-autonomous increase in p53 protein-dependent cell death (Fig. 5*M*).

Excision of *Polr1a*, *Polr1c*, and *Tcof1* Results in Decreased rRNA and Protein Synthesis. Multiple stressors can activate p53 and lead to increased apoptosis or cell-cycle arrest, and the degree of
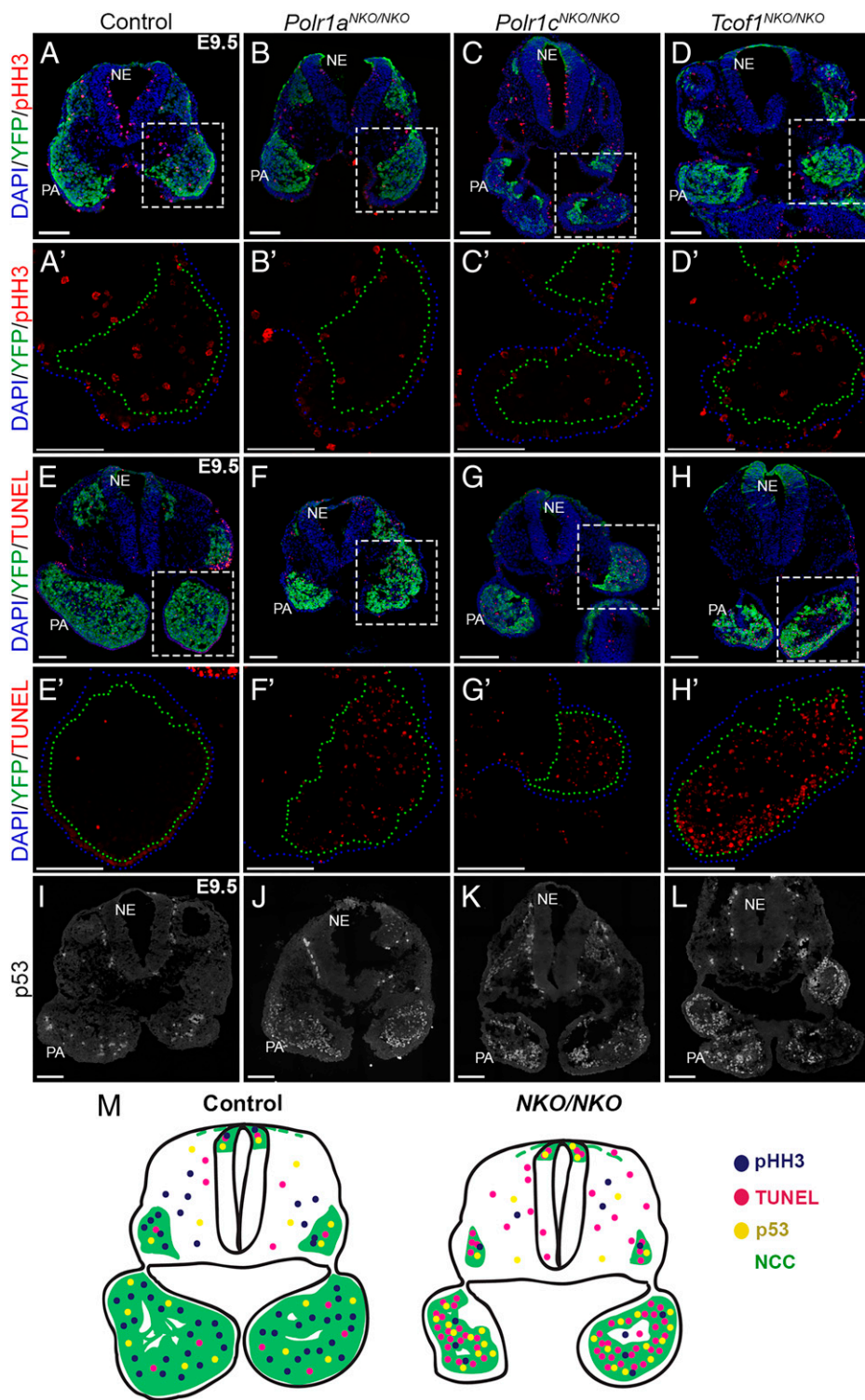
Fig. 5. Reduced proliferation and increased p53-dependent cell death underlies the reduced NCC population in $Polr1a^{NKO/NKO}$, $Polr1c^{NKO/NKO}$, and $Tcof1^{NKO/NKO}$ mice. (A–D) Proliferation (pHH3; red) is reduced in NCC (YFP+) of $Polr1a^{NKO/NKO}$, $Polr1c^{NKO/NKO}$, and $Tcof1^{NKO/NKO}$ embryos. (A′–D′) Higher-magnification view of boxed region in A–D. Pharyngeal arches are outlined in green, indicative of the YFP-expressing cell boundary, and blue, indicative of DAPI-labeled cell boundary. (E–H) TUNEL staining shows increased cell death in YFP+ NCC in the pharyngeal arches of $Polr1a^{NKO/NKO}$, $Polr1c^{NKO/NKO}$, and $Tcof1^{NKO/NKO}$ embryos at E10.5. (E′–H′) Higher magnification of the pharyngeal arches, with the YFP-expressing region outlined in green and DAPI with blue. (I–L) Increased p53 staining (white) in the pharyngeal arches in $Polr1a^{NKO/NKO}$, $Polr1c^{NKO/NKO}$, and $Tcof1^{NKO/NKO}$ embryos suggests p53-dependent cell death. (M) Summary schematic of control and NCC-specific mutant (representative of $Polr1a^{NKO/NKO}$, $Polr1c^{NKO/NKO}$, and $Tcof1^{NKO/NKO}$) sections depicting decreased levels of pHH3 (blue), increased cell death (pink), and p53 (yellow) levels within NCC (green). NE, neuroepithelium; PA, pharyngeal arches. (Scale bars, 100 μm).

p53 activation may contribute to the tissue specificity of developmental syndromes (47). Given the essential role of Pol I subunits and associated factor Treacle in rRNA transcription, we hypothesized that p53 is activated in the *NKO* mutants through a ribosomal stress or nucleolar surveillance response (15, 27, 28). When rRNA transcription is disrupted, this could lead to an imbalance in ribosomal protein to rRNA production, triggering p53 activation. To determine if disruptions in rRNA transcription underlie the increased p53-dependent cell death observed in *NKO* mutants, we analyzed rRNA transcription in fluorescence-activated cell (FAC)-sorted NCCs by qPCR. At E9.5, ~24 h after

Cre excision, 5′ETS expression was significantly down-regulated in $Polr1a^{NKO/NKO}$;*ROSAeYFP* and $Tcof1^{NKO/NKO}$;*ROSAeYFP* NCC when compared with respective control NCCs (Fig. 6A). While 5′ETS was not significantly changed in $Polr1c^{NKO/NKO}$;*ROSAeYFP* NCC compared with controls, 28S rRNA, which reflects the level of the precursor 47S transcript and the mature 28S rRNA, was significantly reduced (Fig. 6A). Overall, our data demonstrate that rRNA transcription begins to decrease in *Polr1a*, *Polr1c*, and *Tcof1 NKO* mutants as early as E9.5.

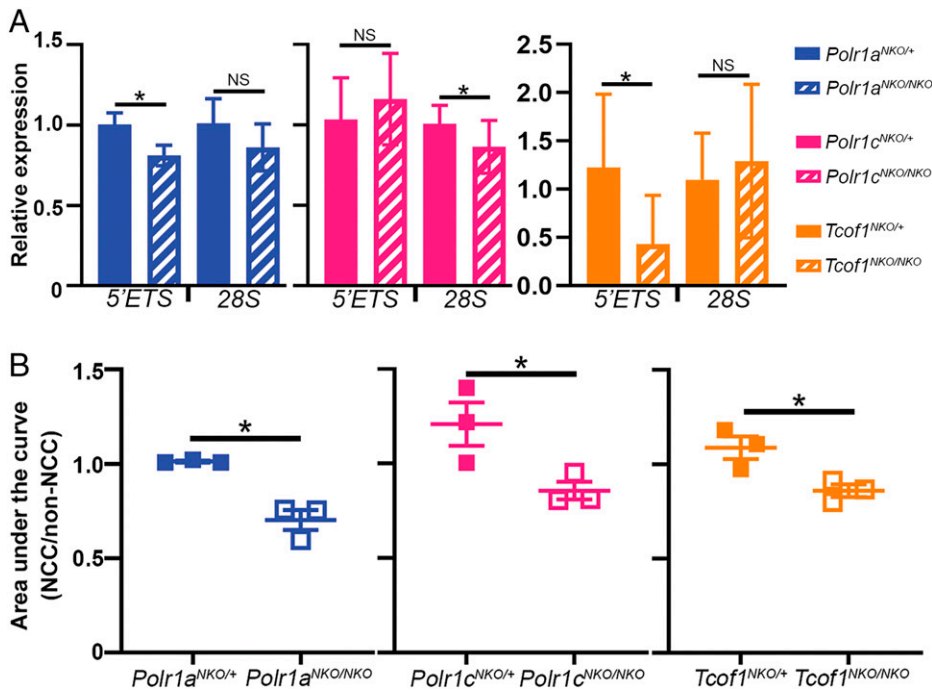Previous studies have shown that reductions in rRNA transcription result in reduced ribosome biogenesis and protein

Fig. 6. rRNA transcription and total protein are reduced in NCCs in $Polr1a^{NKO/NKO}$, $Polr1c^{NKO/NKO}$, and $Tcof1^{NKO/NKO}$ mice. (*A*) qPCR for the 5′ETS region of rRNA is significantly reduced in the sorted NCCs of $Polr1a^{NKO/NKO}$ and $Tcof1^{NKO/NKO}$ embryos, while the mature 28S rRNA transcript is not significantly changed. In $Polr1c^{NKO/NKO}$ embryos, 28S rRNA is reduced, while 5′ETS is not significantly affected. (*B*) Quantification of silver staining demonstrates that the total protein in NCCs is significantly reduced compared with non-NCCs in $Polr1a^{NKO/NKO}$, $Polr1c^{NKO/NKO}$, and $Tcof1^{NKO/NKO}$ embryos at E10.5. A total of 2,000 cells of the YFP+ and YFP− populations of each genotype were used to perform silver staining. NS, not significant. $*P < 0.05$.

synthesis (29), demonstrating that rRNA transcription is a rate-limiting step in ribosome biogenesis. We therefore hypothesized that protein synthesis would be reduced in *Polr1a*, *Polr1c*, and *Tcof1 NKO* NCC as a consequence of reduced rRNA transcription. Protein was extracted from equal numbers of FAC-sorted NCC (YFP+) and non-NCC (YFP−) cells from E10.5 $Polr1a^{NKO/NKO}$;*ROSAeYFP*, $Polr1c^{NKO/NKO}$;*ROSAeYFP*, and $Tcof1^{NKO/NKO}$;*ROSAeYFP* mutant embryos and their respective controls. Silver staining (49) revealed a significant decrease in total protein in *Polr1a*, *Polr1c*, and *Tcof1* NKO NCCs relative to control NCCs (Fig. 6*B* and *SI Appendix*, Fig. S11). This demonstrates that *Polr1a*, *Polr1c*, and *Tcof1* loss-of-function in NCC leads to a cell-autonomous reduction in rRNA transcription and total protein, which results in increased p53-dependent NCC apoptosis and, consequently, craniofacial anomalies.

***Polr1a*, *Polr1c*, and *Tcof1* Deletion Results in Rpl5 and Rpl11 Binding to Mdm2 and p53 Stabilization.** To investigate the molecular mechanism by which Pol I disruption activates p53-dependent apoptosis, we generated mouse embryonic fibroblasts (MEFs) from $Polr1a^{flx/flx}$, $Polr1c^{flx/flx}$, and $Tcof1^{flx/flx}$ mice crossed to tamoxifen-inducible *Cre-ER^{T2}* mice, hereafter referred to as tamoxifen-inducible knockouts (*tKOs*). We observed recombination in nearly 70% of the $Polr1a^{tKO/tKO}$, $Polr1c^{tKO/tKO}$, and $Tcof1^{tKO/tKO}$ cells 24 h after tamoxifen treatment (*SI Appendix*, Fig. S12 *A–C*). As expected, *Polr1a*, *Polr1c*, and *Tcof1* transcripts were decreased in $Polr1a^{tKO/tKO}$, $Polr1c^{tKO/tKO}$, and $Tcof1^{tKO/tKO}$ MEFs compared with $Polr1a^{flx/flx}$, $Polr1c^{flx/flx}$, and $Tcof1^{flx/flx}$ control MEFs 48 h after tamoxifen-induced Cre activation (*SI Appendix*, Fig. S12 *D–F*). Consequently, rRNA transcripts, labeled with the Y10b antibody, were significantly down-regulated in the nucleolus and cytoplasm of *tKO* mutant MEFs (*SI Appendix*, Fig. S12*G*), as was nascent protein synthesis (*SI Appendix*, Fig. S12*H*). At the same time, the levels of p53 were, conversely, increased in $Polr1a^{tKO/tKO}$, $Polr1c^{tKO/tKO}$, and $Tcof1^{tKO/tKO}$ MEFs (*SI Appendix*, Fig. S13), demonstrating the mechanistic equivalency between *tKO* MEFs and *NKO* embryos.

During normal cell growth and proliferation, p53 typically exhibits a short half-life, due in large part to MDM2, which binds to and ubiquitinates p53, targeting it for degradation (50). Mdm2 prevents the accumulation of excess p53, even under conditions of cell stress. However, it has been proposed from in vitro studies that when there is an imbalance in the normal stoichiometric ratio of rRNA and ribosomal proteins, free or excess ribosomal proteins, particularly Rpl5 (uL18) and Rpl11 (uL5), bind to Mdm2, inhibiting its function (24, 51–54). rRNA transcription is decreased in *NKO* embryos and *tKO* MEFs; however, Western blots showed that the levels of Mdm2, and ribosomal proteins Rpl5 and Rpl11, remain unchanged in *tKO* MEFs compared with controls (*SI Appendix*, Fig. S13). Interestingly, immunoprecipitation followed by immunoblotting revealed increased binding of Rpl5 and Rpl11 to Mdm2, in concert with decreased binding between Mdm2 and p53 in *tKO* MEFs compared with controls (Fig. 7). These results suggest that disruptions in Pol I–mediated rRNA transcription alter the stoichiometric balance between rRNA and ribosomal proteins, resulting in increased Rpl5 and Rpl11 binding to Mdm2. This diminishes Mdm2 binding and ubiquitinating p53, leading to tissue-specific p53 accumulation, which can account for the tissue-specific neuroepithelial cell and NCC apoptosis, reduction in NCCs, and craniofacial anomalies characteristic of many ribosomopathies (*SI Appendix*, Fig. S14).

Discussion

rRNA transcription is essential for normal embryo development, and our mouse knockouts of *Polr1a*, *Polr1c*, *Polr1d*, and *Tcof1* demonstrate that Pol I function is critical for preimplantation whole-embryo survival, as well as tissue-specific NCC survival. However, why craniofacial development is highly sensitive to perturbations in global rRNA transcription and Pol I function in humans and animal models (15, 17, 26, 28) remains a critical gap in our knowledge.

Our data demonstrate that rRNA synthesis is tissue-specifically regulated in vivo during mouse embryogenesis and
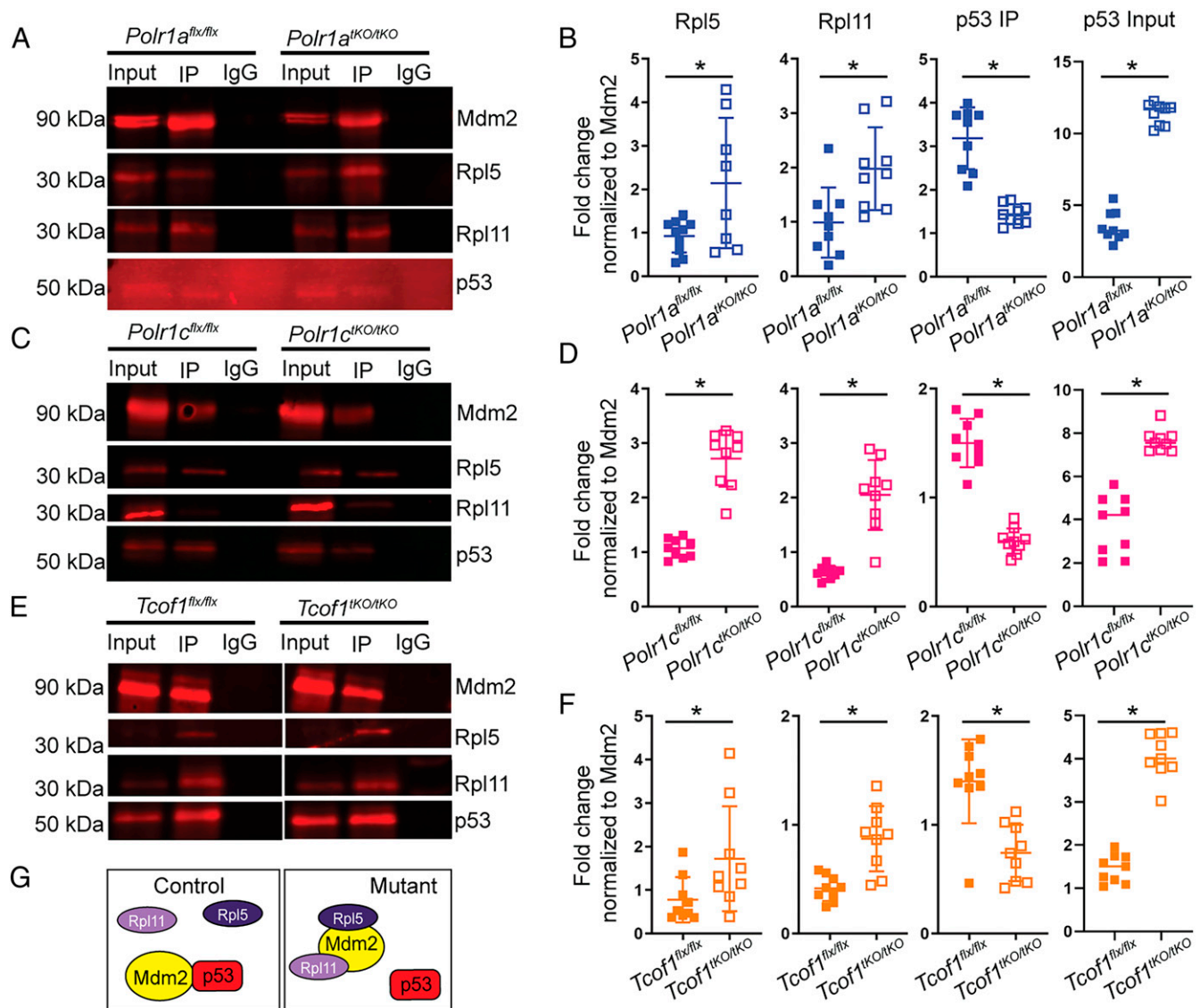
Fig. 7. p53 is activated as a result of higher ribosomal protein binding to Mdm2 in mutant MEFs. MEFs derived from *Polr1a*$^{flx/flx}$, *Polr1a*$^{tKO/tKO}$ (*A* and *B*), *Polr1c*$^{flx/flx}$, *Polr1c*$^{tKO/tKO}$. (*C* and *D*), *Tcof1*$^{flx/flx}$, and *Tcof1*$^{tKO/tKO}$ (*E* and *F*) embryos were treated with tamoxifen and used for immunoprecipitation (IP) assays. Pull-down with Mdm2 and immunoblotting for Rpl5 and Rpl11 revealed increased binding of Mdm2–Rpl5 and Mdm2–Rpl11 in *Polr1a*$^{tKO/tKO}$, *Polr1c*$^{tKO/tKO}$, and *Tcof1*$^{tKO/tKO}$ MEFs compared with their respective control MEFs. Conversely, p53 binding to Mdm2 is reduced in *Polr1a*$^{tKO/tKO}$, *Polr1c*$^{tKO/tKO}$, and *Tcof1*$^{tKO/tKO}$ MEFs compared with controls, consistent with the increased levels of p53 observed in the *Polr1a*$^{NKO/NKO}$, *Polr1c*$^{NKO/NKO}$, and *Tcof1*$^{NKO/NKO}$ embryos. Band intensities were measured as the ratio between Mdm2 and Rpl5, Rpl11, or p53. (*G*) Summary schematic showing Mdm2–p53 binding in control and Rpl5, Rpl11–Mdm2 binding in mutant resulting in free p53. *$P < 0.05$, Student's *t* test.

that this correlates with tissue-specific threshold sensitivities to disruptions in rRNA transcription. Quantification of 47S pre-rRNA transcription showed that the neuroepithelium and NCCs exhibit endogenously high levels of rRNA transcription compared with surrounding non-NCCs (Fig. 1 and *SI Appendix*, Fig. S14A versus *SI Appendix*, Fig. S14C), which is mechanistically underpinned by dynamically enriched expression of *Tcof1*, *Polr1a*, *Polr1c*, *Polr1d*, and other Pol I subunit transcripts and protein in the neuroepithelium and NCCs in mice (Fig. 2 and *SI Appendix*, Fig. S4). This correlates with elevated translation in the neuroepithelium and NCC progenitors, which is necessary to meet high proliferation needs and possibly other demands, such as the requirement to translate new proteins for cytoskeletal rearrangement during epithelial-to-mesenchymal transitions (EMTs) (55) (Fig. 1 and *SI Appendix*, Figs. S1 and S14A).

Global disruption of Pol I transcription using BMH-21 results in apoptosis specifically in neuroepithelial cells and NCC

progenitors in E8.5 mouse embryos (Fig. 1 *J–L*). Further, craniofacial anomalies are more severe and 100% penetrant in *Tcof1*$^{+/-}$; *Polr1a*$^{+/-}$, *Tcof1*$^{+/-}$;*Polr1c*$^{+/-}$, and *Tcof1*$^{+/-}$;*Polr1d*$^{+/-}$ double heterozygous mutants compared with craniofacial anomalies observed in *Tcof1*$^{+/-}$ mutant embryos (Fig. 3). Therefore, taken together with our previous observations in zebrafish (15, 28), this indicates that high rRNA transcription in NCC progenitors leads to their high sensitivity to disruptions in rRNA synthesis, while non-NCC-derived tissues are affected to a lesser degree (Fig. 3 and *SI Appendix*, Fig. S14B versus *SI Appendix*, Fig. S14D).

Furthermore, Pol I-mediated transcription functions in a cell-autonomous manner during mouse NCC development. NCC-specific deletion of *Polr1a*, *Polr1c*, and *Tcof1* genes results in NCC-autonomous down-regulation of rRNA transcription (Fig. 6), leading to increased p53-dependent cell death (Fig. 5) and, consequently, craniofacial anomalies (Fig. 4). While mechanistically similar, there are subtle differences between *Polr1a*$^{NKO/NKO}$, *Polr1c*$^{NKO/NKO}$, and *Tcof1*$^{NKO/NKO}$ embryos.

For example, the NCC population is more severely reduced in $Polr1a^{NKO/NKO}$ embryos compared with $Polr1c^{NKO/NKO}$ (Fig. 4), corresponding with previous work in zebrafish (15, 28). $Tcof1^{NKO/NKO}$ embryos exhibit the least severe phenotype in comparison with $Polr1a^{NKO/NKO}$ and $Polr1c^{NKO/NKO}$. This is consistent with Polr1a forming part of the catalytic site of Pol I, whereas Polr1c functions to hold Polr1a and Polr1b together, but does not form part of the catalytic site, while Tcof1/Treacle is an associated factor that interacts with Pol I (56). Interestingly, while Polr1a is a component of Pol I only, Polr1c is a subunit of both Pol I and Pol III and, therefore, may impact Pol III transcription in addition to Pol I, resulting in differences in how rRNA transcription is affected in NCCs (Fig. 6A). Modeling of pathogenic variants in *POLR1C* in HeLa cells suggests that the variants associated with TCS primarily affect Pol I function (57), although studies modeling similar pathogenic variants in yeast have indicated that some TCS variants can affect both Pol I and Pol III (25). The role of Pol III in NCCs and craniofacial development is an interesting area for future investigation, and it remains to be determined whether this also involves p53-dependent effects.

Tcof1/Treacle, however, does have additional roles to its function in rRNA transcription, namely, in reactive oxygen species-induced DNA damage repair (*SI Appendix*, Fig. S5 and Table S1), which, when perturbed, can also lead to p53-dependent apoptosis (21, 58, 59). Consistent with this known role of Tcof1/Treacle in DNA damage repair (21), we detected γ-H2AX expression in the pharyngeal arches of $Tcof1^{NKO/NKO}$ mutants and in $Tcof1^{tKO/tKO}$ MEFs (*SI Appendix*, Fig. S15 *D and H*). However, γ-H2AX only labeled a minority of NCCs in $Tcof1^{NKO/NKO}$ mutants, suggesting that Tcof1/Treacle's function in DNA damage repair is secondary to its primary role in rRNA transcription (21, 60). Moreover, antioxidant treatment to reduce reactive oxygen species-induced DNA damage ameliorates the craniofacial anomalies in about 30% of $Tcof1^{+/-}$ mice (21), but a much higher percentage (75%) are rescued via genetic p53 inhibition (27), again indicating that Tcof1/Treacle is mainly required for rRNA transcription (60). In contrast, we observed no evidence for γ-H2AX–labeled double-strand breaks in $Polr1a^{NKO/NKO}$ or $Polr1c^{NKO/NKO}$ mutant embryos (*SI Appendix*, Fig. S15 *B and C*) and $Polr1a^{tKO/tKO}$ or $Polr1c^{tKO/tKO}$ MEFs (*SI Appendix*, Fig. S15 *F and G*). Thus, the TUNEL staining observed in association with Polr1a and Polr1c loss-of-function is not due to DNA damage. Therefore, given that p53 was increased in all the *NKO* embryos (Fig. 5) and *tKO* mutant MEFs (*SI Appendix*, Fig. S13), this further substantiates the correlation between deficiencies in rRNA transcription and the Rpl5/11–Mmd2–p53-mediated tissue-specific apoptotic effects on NCCs in the pathogenesis of ribosomopathy-associated craniofacial anomalies. Altogether, while there is more to learn about the ribosomal and extraribosomal functions of Pol I subunits and associated factors, it remains clear that *Polr1a*, *Polr1c*, and *Tcof1* are required in NCCs and that the phenotypes of the $Polr1a^{NKO/NKO}$, $Polr1c^{NKO/NKO}$, and $Tcof1^{NKO/NKO}$ embryos are unified by perturbation of rRNA transcription and an increase in p53-dependent cell death.

While p53 signaling has been implicated in multiple ribosomopathies (45) and developmental syndromes (47), how disruptions in rRNA transcription and ribosome biogenesis result in cell-type-specific apoptosis and the molecular mechanism underlying elevated p53 levels in different pathologies remains unclear (24). Contrary to previous literature that implicates higher transcription of *p53* in the NCCs compared with surrounding cells as a potential reason for neurocristopathies (46),

we observe that *p53* transcript quantity is similar in NCCs and other craniofacial cell types during early embryogenesis (*SI Appendix*, Fig. S10). In addition, previous data show that p53 protein levels are uniformly low in the neuroepithelium and surrounding tissues in wild-type embryos (27). However, in the absence of Pol I subunits or *Tcof1*, p53 protein is up-regulated in a tissue-specific manner (Fig. 5 and *SI Appendix*, Figs. S9 and S10). We demonstrate that posttranslational p53 activation in *Polr1a*, *Polr1c*, and *Tcof1* loss-of-function mutants results from an imbalance between rRNA transcription and ribosomal proteins, triggering a nucleolar surveillance response. Excess Rpl5 and Rpl11 bind to Mdm2, limiting Mdm2's ability to bind and ubiquitinate p53 (Fig. 7), which leads to p53 protein accumulation and, ultimately, NCC death (Fig. 5 and *SI Appendix*, Fig. S14). Further contributing to the tissue-specific impact of perturbed rRNA transcription and p53-dependent activation is that different tissues, including the neuroepithelium and cultured cranial NCCs, may be more sensitive to p53 activation (46) and, therefore, likely to undergo cell death in response to p53 activation (47), as opposed to other responses to p53 activation, such as cell-cycle arrest or senescence, the latter of which we did not observe. Our work therefore suggests that the initial trigger for p53 activation and accumulation in the neuroepithelium in TCS or AFDCIN may be through a nucleolar surveillance mechanism and that the sensitivity of the neuroepithelium and NCCs to p53 activation arises, at least in part, from their elevated requirement for rRNA transcription (*SI Appendix*, Fig. S14). Consistent with this model, the levels of rRNA transcription correlate with their susceptibility to p53-dependent cell death in cancer cell lines. Cancer cells with relatively high levels of rRNA transcription tend to undergo cell death after inhibition of rRNA synthesis, whereas cells with relatively low levels of rRNA transcription undergo cell-cycle arrest and are more likely to survive (24). Altogether, a nucleolar surveillance mechanism may also contribute to other ribosomopathies, in which deficiencies in specific ribosomal proteins or increased rRNA transcription (61) are associated with p53-dependent cell death (62, 63). Moreover, it emphasizes the importance of balanced rRNA and ribosomal protein production in the pathogenesis of these pathologies.

Our data suggest that the tissue-specific regulation of rRNA transcription has important implications across multiple diseases and tissue types. While tissue-specific expression and function of ribosomal proteins and preribosomal factors contribute to the pathogenesis of several developmental ribosomopathies (64, 65), the dynamic cell- and tissue-specific regulation of rRNA expression during development is not as well understood. Recent studies have observed tissue-specific expression of rRNA in the mouse eye and ovary (32, 33), during forebrain development (66), and during EMTs (55, 64). The level of rRNA in these tissues was hypothesized to correlate with levels of proliferation, similar to our data for the neuroepithelium and NCCs in E8.5 embryos. Interestingly, the differential levels of rRNA transcription in NCCs compared with surrounding cells begins to decrease by E9.5, suggesting that NCC progenitors are more sensitive during their formation, proliferation, and migration stages of development, than later during differentiation. Consistent with this idea, reductions in rRNA transcription have been observed in association with differentiation in other systems (66–68).

Other factors may also contribute to dynamic tissue-specific rRNA transcription beyond a proliferation and survival versus differentiation demand. This includes epigenetic changes in rDNA (69), rDNA copy-number variation (70), tissue-specific

expression of variant rRNA alleles (69), or regulation of rRNA synthesis by transcription factors such as Snail1 (55) and Runx2 (71), which are involved in EMTs or osteochondroprogenitor differentiation, respectively. Our data suggest that endogenous differential Pol I subunit and *Tcof1* gene expression contribute to the dynamic tissue-specific regulation of rRNA, which underlies the craniofacial defects in TCS and AFDCIN. However, further work is needed to determine the upstream mechanisms that modulate the expression of Pol I and Pol I–mediated transcription, especially in the context of development and disease.

In summary, our work has uncovered a dynamic tissue-specific regulation and requirement for rRNA transcription during mammalian embryonic development, which mechanistically accounts for the corresponding tissue-specific threshold sensitivities to disruptions in rRNA transcription, particularly in NCCs during craniofacial development. Loss-of-function of Pol I catalytic subunit (Polr1a), noncatalytic subunit (Polr1c), and associated factor (Tcof1) result in similar phenotypes, illustrating the conserved mechanisms underpinning the etiology and pathogenesis of Pol I-related craniofacial birth defects in ribosomopathies, such as TCS and AFDCIN. Furthermore, we found that the rRNA–Rpl5/Rpl11–Mdm2–p53 molecular pathway, which has been previously studied in the context of cancer in yeast and cell lines (24, 53), accounts for the post-translational activation of p53 protein in response to perturbed rRNA transcription. This explains why p53 inhibition is able to suppress apoptosis and rescue craniofacial anomalies in mouse (27) and zebrafish (28, 29) models of rRNA transcription deficiency and raises the possibility that re-establishing the stochiometric ratio between rRNAs and ribosomal proteins could provide a broadly applicable avenue for the therapeutic prevention of ribosomopathies.

Materials and Methods

Animal Husbandry. All mice were housed in a 16h-light:8h-dark light cycle. All animal experiments were conducted in accordance with Stowers Institute for Medical Research Institutional Animal Care and Use Committee (IACUC)-approved protocol (IACUC no. 2019-097). Transgenic mouse lines were generated at the Stowers Institute for Medical Research Laboratory Animal Facility or by the Virginia Commonwealth University Transgenic/Knockout Mouse Facility (Virginia Commonwealth University IACUC no. AM10025). Details of their generation and maintenance can be found in *SI Appendix, Materials and Methods*. MEFs were derived from transgenic mice as described (72).

Molecular and Phenotypic Analysis. Skeletal staining, in situ hybridization, and immunohistochemistry were performed according to published methods (73, 74). Descriptions of RNA and proteomic assays, along with quantification and statistical analyses, are provided in *SI Appendix, Materials and Methods*.

Data Availability. Original data underlying this manuscript can be accessed from the Stowers Original Data Repository (https://www.stowers.org/research/publications/LIBPB-1604) (75). PyImageJ scripts that interface with ImageJ from Jupyter Notebooks and which are noted in the methods and were used for quantitative analyses can also be found there. Single-cell RNA-sequencing data have been deposited in the Gene Expression Omnibus (accession no. 168351) (76). All study data are included in the article and/or *SI Appendix*.

Author affiliations: [a]Stowers Institute for Medical Research, Kansas City, MO 64110; [b]Department of Anatomy and Cell Biology, University of Kansas Medical Center, Kansas City, KS 66160; [c]Department of Biology, Kanazawa Medical University, Uchinada, Ishikawa 920-0293, Japan; [d]Department of Biostatistics and Data Science, University of Kansas Medical Center, Kansas City, KS 66160; [e]Department of Orthopedic Surgery, Stanford University, Stanford, CA 94305; [f]Department of Human and Molecular Genetics, Virginia Commonwealth University, Richmond, VA 23284; [g]Department of Basic and Clinical Sciences, University of Nicosia Medical School, Nicosia 2408, Cyprus; and [h]Faculty of Biology, Medicine, and Health, University of Manchester, Manchester M13 9PL, United Kingdom

Author contributions: K.T.F., K.E.N.W., S.D., R.Z., D.S., E.L.M., S.F., M.E.S., S.S., R.S., A.A., J.D., M.J.D., and P.A.T. designed research; K.T.F., K.E.N.W., S.D., R.Z., D.S., E.L.M., S.F., M.C., D.T., G.B., L.L., R.S., A.A., and P.A.T. performed research; K.T.F., K.E.N.W., S.D., R.Z., D.S., E.L.M., S.F., M.E.S., S.S., D.T., J.U., L.L., R.S., A.A., J.D., M.J.D., and P.A.T. contributed new reagents/analytic tools; K.T.F., K.E.N.W., S.D., R.Z., D.S., E.L.M., S.F., M.C., M.E.S., S.S., D.T., J.U., G.B., L.L., R.S., A.A., and P.A.T. analyzed data; and K.T.F., K.E.N.W., S.D., R.Z., D.S., E.L.M., S.F., M.E.S., R.S., A.A., J.D., M.J.D., and P.A.T. wrote the paper.

1. P. A. Trainor, A. E. Merrill, Ribosome biogenesis in skeletal development and the pathogenesis of skeletal disorders. *Biochim. Biophys. Acta* **1842**, 769–778 (2014).
2. P. Jorgensen et al., A dynamic transcriptional network communicates growth potential to ribosome synthesis and critical cell size. *Genes Dev.* **18**, 2491–2505 (2004).
3. T. Chaillou, T. J. Kirby, J. J. McCarthy, Ribosome biogenesis: Emerging evidence for a central role in the regulation of skeletal muscle mass. *J. Cell. Physiol.* **229**, 1584–1594 (2014).
4. C. B. Kirn-Safran et al., Global growth deficiencies in mice lacking the ribosomal protein HIP/RPL29. *Dev. Dyn.* **236**, 447–460 (2007).
5. G. Thomas, An encore for ribosome biogenesis in the control of cell proliferation. *Nat Cell Biol.* **2**, E71–E72 (2000).
6. A. Laferté et al., The transcriptional activity of RNA polymerase I is a key determinant for the level of all ribosome components. *Genes Dev.* **20**, 2030–2040 (2006).
7. S. Chédin et al., Is ribosome synthesis controlled by pol I transcription? *Cell Cycle* **6**, 11–15 (2007).
8. J. R. Warner, The economics of ribosome biosynthesis in yeast. *Trends Biochem. Sci.* **24**, 437–440 (1999).
9. A. D. Misiaszek et al., Cryo-EM structures of human RNA polymerase I. *Nat. Struct. Mol. Biol.* **28**, 997–1008 (2021).
10. Y. S. Polikanov, S. V. Melnikov, D. Söll, T. A. Steitz, Structural insights into the role of rRNA modifications in protein synthesis and ribosome assembly. *Nat. Struct. Mol. Biol.* **22**, 342–344 (2015).
11. S. O. Sulima, K. R. Kampen, K. De Keersmaecker, Cancer biogenesis in ribosomopathies. *Cells* **8**, 229 (2019).
12. N. Danilova, H. T. Gazda, Ribosomopathies: How a common root can cause a tree of pathologies. *Dis. Model. Mech.* **8**, 1013–1026 (2015).
13. P. C. Yelick, P. A. Trainor, Ribosomopathies: Global process, tissue specific defects. *Rare Dis.* **3**, e1025185 (2015).
14. E. W. Mills, R. Green, Ribosomopathies: There's strength in numbers. *Science* **358**, eaan2755 (2017).
15. K. N. Weaver et al., Acrofacial dysostosis, Cincinnati type, a mandibulofacial dysostosis syndrome with limb anomalies, is caused by POLR1A dysfunction. *Am. J. Hum. Genet.* **96**, 765–774 (2015).
16. J. G. Dauwerse et al., Mutations in genes encoding subunits of RNA polymerases I and III cause Treacher Collins syndrome. *Nat. Genet.* **43**, 20–22 (2011).
17. K. Terrazas, J. Dixon, P. A. Trainor, M. J. Dixon, Rare syndromes of the head and face: Mandibulofacial and acrofacial dysostoses. *Wiley Interdiscip. Rev. Dev. Biol.*, 10.1002/wdev.263 (2017).
18. P. A. Trainor, J. Dixon, M. J. Dixon, Treacher Collins syndrome: Etiology, pathogenesis and prevention. *Eur. J. Hum. Genet.* **17**, 275–283 (2009).
19. B. Gonzales et al., The Treacher Collins syndrome (TCOF1) gene product is involved in pre-rRNA methylation. *Hum. Mol. Genet.* **14**, 2035–2043 (2005).
20. B. C. Valdez, D. Henning, R. B. So, J. Dixon, M. J. Dixon, The Treacher Collins syndrome (TCOF1) gene product is involved in ribosomal DNA gene transcription by interacting with upstream binding factor. *Proc. Natl. Acad. Sci. U.S.A.* **101**, 10709–10714 (2004).
21. D. Sakai, J. Dixon, A. Achilleos, M. Dixon, P. A. Trainor, Prevention of Treacher Collins syndrome craniofacial anomalies in mouse models via maternal antioxidant supplementation. *Nat. Commun.* **7**, 10328 (2016).
22. S. Bhatt, R. Diaz, P. A. Trainor, Signals and switches in Mammalian neural crest cell differentiation. *Cold Spring Harb. Perspect. Biol.* **5**, a008326 (2013).
23. A. Achilleos, P. A. Trainor, Mouse models of rare craniofacial disorders. *Curr. Top. Dev. Biol.* **115**, 413–458 (2015).
24. F. Scala et al., Direct relationship between the level of p53 stabilization induced by rRNA synthesis-inhibiting drugs and the cell ribosome biogenesis rate. *Oncogene* **35**, 977–989 (2016).
25. N. Walker-Kopp et al., Treacher Collins syndrome mutations in Saccharomyces cerevisiae destabilize RNA polymerase I and III complex integrity. *Hum. Mol. Genet.* **26**, 4290–4300 (2017).
26. J. Dixon et al., Tcof1/Treacle is required for neural crest cell formation and proliferation deficiencies that cause craniofacial abnormalities. *Proc. Natl. Acad. Sci. U.S.A.* **103**, 13403–13408 (2006).
27. N. C. Jones et al., Prevention of the neurocristopathy Treacher Collins syndrome through inhibition of p53 function. *Nat. Med.* **14**, 125–133 (2008).

28. K. E. Noack Watt, A. Achilleos, C. L. Neben, A. E. Merrill, P. A. Trainor, The roles of RNA polymerase I and III subunits Polr1c and Polr1d in craniofacial development and in zebrafish models of Treacher Collins syndrome. *PLoS Genet.* **12**, e1006187 (2016).

29. K. E. N. Watt, C. L. Neben, S. Hall, A. E. Merrill, P. A. Trainor, tp53-dependent and independent signaling underlies the pathogenesis and possible prevention of acrofacial dysostosis-Cincinnati type. *Hum. Mol. Genet.* **27**, 2628–2643 (2018).

30. E. Sanchez *et al.*, POLR1B and neural crest cell anomalies in Treacher Collins syndrome type 4. *Genet. Med.* **22**, 547–556 (2020).

31. X. You *et al.*, Neural circular RNAs are derived from synaptic genes and regulated by development and plasticity. *Nat. Neurosci.* **18**, 603–610 (2015).

32. J. Qian, R. M. Lavker, H. Tseng, Mapping ribosomal RNA transcription activity in the mouse eye. *Dev. Dyn.* **235**, 1984–1993 (2006).

33. C. Cui, H. Tseng, Estimation of ribosomal RNA transcription rate in situ. *Biotechniques* **36**, 134–138 (2004).

34. Y. Echelard, G. Vassileva, A. P. McMahon, Cis-acting regulatory sequences governing Wnt-1 expression in the developing mouse CNS. *Development* **120**, 2213–2224 (1994).

35. J. Liu, Y. Xu, D. Stoleru, A. Salic, Imaging protein synthesis in cells and tissues with an alkyne analog of puromycin. *Proc. Natl. Acad. Sci. U.S.A.* **109**, 413–418 (2012).

36. L. Colis *et al.*, DNA intercalator BMH-21 inhibits RNA polymerase I independent of DNA damage response. *Oncotarget* **5**, 4361–4369 (2014).

37. L. Florens, M. P. Washburn, Proteomic analysis by multidimensional protein identification technology. *Methods Mol. Biol.* **328**, 159–175 (2006).

38. M. P. Washburn, D. Wolters, J. R. Yates III, Large-scale analysis of the yeast proteome by multidimensional protein identification technology. *Nat. Biotechnol.* **19**, 242–247 (2001).

39. C. Isaac *et al.*, Characterization of the nucleolar gene product, treacle, in Treacher Collins syndrome. *Mol. Biol. Cell* **11**, 3061–3071 (2000).

40. Z. R. Conley *et al.*, A quantitative method for defining high-arched palate using the Tcof1(+/−) mutant mouse as a model. *Dev. Biol.* **415**, 296–305 (2016).

41. J. Dixon, M. J. Dixon, Genetic background has a major effect on the penetrance and severity of craniofacial defects in mice heterozygous for the gene encoding the nucleolar protein Treacle. *Dev. Dyn.* **229**, 907–914 (2004).

42. V. Brault *et al.*, Inactivation of the β-catenin gene by Wnt1-Cre-mediated deletion results in dramatic brain malformation and failure of craniofacial development. *Development* **128**, 1253–1264 (2001).

43. S. Srinivas *et al.*, Cre reporter strains produced by targeted insertion of EYFP and ECFP into the ROSA26 locus. *BMC Dev. Biol.* **1**, 4 (2001).

44. L.-J. Ng *et al.*, SOX9 binds DNA, activates transcription, and coexpresses with type II collagen during chondrogenesis in the mouse. *Dev. Biol.* **183**, 108–121 (1997).

45. S. Fumagalli, G. Thomas, The role of p53 in ribosomopathies. *Semin. Hematol.* **48**, 97–105 (2011).

46. E. Calo *et al.*, Tissue-selective effects of nucleolar stress and rDNA damage in developmental disorders. *Nature* **554**, 112–117 (2018).

47. M. E. Bowen *et al.*, The spatiotemporal pattern and intensity of p53 activation dictates phenotypic diversity in p53-driven developmental syndromes. *Dev. Cell* **50**, 212–228.e6 (2019).

48. P. G. Komarov *et al.*, A chemical inhibitor of p53 that protects mice from the side effects of cancer therapy. *Science* **285**, 1733–1737 (1999).

49. M. Chevallet, S. Luche, T. Rabilloud, Silver staining of proteins in polyacrylamide gels. *Nat. Protoc.* **1**, 1852–1858 (2006).

50. Y. Haupt, R. Maya, A. Kazaz, M. Oren, Mdm2 promotes the rapid degradation of p53. *Nature* **387**, 296–299 (1997).

51. G. Donati *et al.*, The balance between rRNA and ribosomal protein synthesis up- and downregulates the tumour suppressor p53 in mammalian cells. *Oncogene* **30**, 3274–3288 (2011).

52. M. A. E. Lohrum, R. L. Ludwig, M. H. G. Kubbutat, M. Hanlon, K. H. Vousden, Regulation of HDM2 activity by the ribosomal protein L11. *Cancer Cell* **3**, 577–587 (2003).

53. Y. Liu, C. Deisenroth, Y. Zhang, RP-MDM2-p53 pathway: Linking ribosomal biogenesis and tumor surveillance. *Trends Cancer* **2**, 191–204 (2016).

54. D. G. Pestov, Z. Strezoska, L. F. Lau, Evidence of p53-dependent cross-talk between ribosome biogenesis and the cell cycle: Effects of nucleolar protein Bop1 on G(1)/S transition. *Mol. Cell. Biol.* **21**, 4246–4255 (2001).

55. V. Prakash *et al.*, Ribosome biogenesis during cell cycle arrest fuels EMT in development and disease. *Nat. Commun.* **10**, 2110 (2019).

56. C. Engel, S. Sainsbury, A. C. Cheung, D. Kostrewa, P. Cramer, RNA polymerase I structure and transcription regulation. *Nature* **502**, 650–655 (2013).

57. I. Thiffault *et al.*, Recessive mutations in POLR1C cause a leukodystrophy by impairing biogenesis of RNA polymerase III. *Nat. Commun.* **6**, 7623 (2015).

58. A. Ciccia *et al.*, Treacher Collins syndrome TCOF1 protein cooperates with NBS1 in the DNA damage response. *Proc. Natl. Acad. Sci. U.S.A.* **111**, 18631–18636 (2014).

59. D. H. Larsen *et al.*, The NBS1-Treacle complex controls ribosomal RNA transcription in response to DNA damage. *Nat. Cell Biol.* **16**, 792–803 (2014).

60. D. Sakai, P. A. Trainor, Face off against ROS: Tcof1/Treacle safeguards neuroepithelial cells and progenitor neural crest cells from oxidative stress during craniofacial development. *Dev. Growth Differ.* **58**, 577–585 (2016).

61. C. L. Neben, C. T. Tuzon, X. Mao, F. D. Lay, A. E. Merrill, FGFR2 mutations in bent bone dysplasia syndrome activate nucleolar stress and perturb cell fate determination. *Hum. Mol. Genet.* **26**, 3253–3270 (2017).

62. S. Le Goff *et al.*, p53 activation during ribosome biogenesis regulates normal erythroid differentiation. *Blood* **137**, 89–102 (2021).

63. F. Lessard, L. Brakier-Gingras, G. Ferbeyre, Ribosomal proteins control tumor suppressor pathways in response to nucleolar stress. *BioEssays* **41**, e1800183 (2019).

64. A. A. Panoutsopoulos *et al.*, Pak1ip1 loss-of-function leads to cell cycle arrest, loss of neural crest cells, and craniofacial abnormalities. *Front. Cell Dev. Biol.* **8**, 510063 (2020).

65. N. R. Genuth, M. Barna, The discovery of ribosome heterogeneity and its implications for gene regulation and organismal life. *Mol. Cell* **71**, 364–374 (2018).

66. K. F. Chau *et al.*, Downregulation of ribosome biogenesis during early forebrain development. *eLife* **7**, e36998 (2018).

67. J. L. Woolnough, B. L. Atwood, Z. Liu, R. Zhao, K. E. Giles, The regulation of rRNA gene transcription during directed differentiation of human embryonic stem cells. *PLoS One* **11**, e0157276 (2016).

68. Q. Zhang, N. A. Shalaby, M. Buszczak, Changes in rRNA transcription influence proliferation and cell fate within a stem cell lineage. *Science* **343**, 298–301 (2014).

69. M. M. Parks *et al.*, Variant ribosomal RNA alleles are conserved and exhibit tissue-specific expression. *Sci. Adv.* **4**, eaao0665 (2018).

70. D. Salim *et al.*, DNA replication stress restricts ribosomal DNA copy number. *PLoS Genet.* **13**, e1007006 (2017).

71. S. A. Ali *et al.*, A RUNX2-HDAC1 co-repressor complex regulates rRNA gene expression by modulating UBF acetylation. *J. Cell Sci.* **125**, 2732–2739 (2012).

72. J. Xu, Preparation, culture, and immortalization of mouse embryonic fibroblasts. *Curr. Protoc. Mol. Biol.* **70**, 28.21.21–28.21.28 (2005).

73. J. F. Dennis *et al.*, Mutations in Hedgehog acyltransferase (Hhat) perturb Hedgehog signaling, resulting in severe acrania-holoprosencephaly-agnathia craniofacial defects. *PLoS Genet.* **8**, e1002927 (2012).

74. R. Behringer, M. Gertsenstein, V. Nagy, A. Nagy, *Manipulating the Mouse Embryo: A Laboratory Manual* (Cold Spring Harbor Laboratory Press, Cold Spring Harbor, NY, ed. 4, 2014).

75. K. T. Falcon *et al.*, Data from "Dynamic regulation and requirement for ribosomal RNA transcription during mammalian development." Stowers Original Data Repository. https://www.stowers.org/research/publications/LIBPB-1604. Deposited 21 July 2022.

76. K. T. Falcon *et al.*, Data from "Dynamic regulation and requirement for ribosomal RNA transcription during mammalian development." Gene Expression Omnibus. http://www.ncbi.nlm.nih.gov/geo/query/acc.cgi?acc=GSE168351. Deposited 5 March 2021.

Supplementary Information

Materials and Methods

Mice and animal husbandry

Polr1a$^{+/-}$ and Polr1a$^{flx/flx}$

C57BL/6N-*Polr1a$^{tm1a(EUCOMM)Hmgu/BayMmucd}$* mice were obtained from the Mutant Mouse Resource & Research Center and maintained on a C57BL/6 background. The *Polr1a$^{βgeo/+}$* (*Polr1a$^{+/-}$*) gene trap knockout ready mice were originally generated at the Baylor College of Medicine by injecting ES cell clone HEPD0779_7_B03 into C57BL/6J-Tyr blastocysts (1). Resulting male chimeras were mated to C57BL/6N females, and the progeny were maintained on a C57BL/6N background. *Polr1a^{tm1a}* (*Polr1a$^{+/-}$*) mice were crossed to FlpO (B6.129S4-*Gt(ROSA)26Sor$^{tm2(FLP*)Sor}$*/J, Jax Stock# 012930) mice (2) to generate *Polr1a$^{flx/+}$* mice which were maintained on a C57BL/6 background and then incrossed to generate *Polr1a$^{flx/flx}$* mice (Fig. S3)

Polr1c$^{+/-}$ and Polr1c$^{flx/flx}$

The *Polr1c$^{tm1a(KOMP)Wtsi}$* ES cells used to generate the *Polr1c$^{βgeo/+/-}$* (*Polr1c$^{+/-}$*) gene trap knockout ready mouse strain were obtained from the Knock-out mouse project (KOMP) repository. The C57BL/6N parental ES cell line JM8A3.N1 was injected into C57BL/6 blastocysts at the Stowers Institute for Medical Research Laboratory Animal Facility and the *Polr1c$^{+/-}$* gene trap line was established and maintained on a C57BL/6 background. To generate the *Polr1c$^{flx/flx}$* line, mice carrying the FLP recombinase (FLPeR) in the *Rosa26* locus were crossed to the *Polr1c$^{+/-}$* gene trap mice and the resulting *Polr1c$^{flx/+}$* mice were incrossed to homozygosity. The *FLPeR* (B6.129S4-*Gt(ROSA)26Sor$^{tm1(FLP1)Dym}$*/RainJ, Jax stock #009086) mice were obtained from Jackson Laboratory.

Polr1d$^{βgeo/+}$ (*Polr1d$^{+/-}$*)

A C57BL/6 ES cell line (IST10113B8) with a *βgeo* gene trap vector inserted into exon 1 of the *Polr1d* gene was obtained from Texas A&M Institute for Genomic Medicine and injected into C57BL/6 blastocysts at the Stowers Laboratory Animal Facility. *Polr1d$^{+/-}$* mice were maintained on a C57BL/6 background.

Tcof1$^{+/-}$ and Tcof1$^{flx/flx}$

Tcof1$^{+/-}$ mice were generated by insertion of neomycin cassette in exon 1 and maintained as previously described (3) on a DBA background. To generate a conditional allele of *Tcof1,* exon 1 of *Tcof1* was flanked by loxP sites using the targeting vector pTKLNCDL (a gift from Dr. Richard Mortensen) containing a neomycin cassette and loxP sites. The construct was electroporated into ES cells in 129/SvEv ES (HZ2.2) cells and the ES cells that underwent homozygous recombination were cultured and transiently transfected with 7μg of pCMV-cre by electroporation to remove the neomycin cassette, leaving two loxP sites flanking exon 1. This recombination in ES cells was confirmed by PCR and Southern blotting and

the cells were injected into C57BL/6 blastocysts to generate *Tcof1*^{flx/+} mice by the Virginia Commonwealth University Transgenic/Knockout Mouse Facility (Virginia Commonwealth University IACUC #AM10025). These mice were then backcrossed onto a C57BL/6 background.

Mef2c-F10N-LacZ

Mef2c-F10N-LacZ mice in which LacZ is expressed under the control of a neural crest cell specific enhancer of *Mef2c* were maintained as previously described (4).

Double Heterozygote Generation

Tcof1$^{+/-}$ mice were crossed to *Polr1a*$^{+/-}$, *Polr1c*$^{+/-}$, or *Polr1d*$^{+/-}$ mice carrying a heterozygous gene trap allele described above.

Neural Crest Cell knockouts and lineage tracing

Wnt1-Cre mice (*H2afv*$^{Tg(Wnt1-cre)11Rth}$ Tg(Wnt1-GAL4)11Rth/J, Jax stock #003829) and *RosaeYFP* mice were obtained from the Jackson Laboratory and maintained as previously described (5, 6). *Polr1a*$^{flx/flx}$, *Polr1c*$^{flx/flx}$, and *Tcof1*$^{flx/flx}$ mice were crossed to *Wnt1-Cre* transgenic mice to generate *Polr1a*$^{flx/+}$;*Wnt1-Cre*, *Polr1c*$^{flx/+}$;*Wnt1-Cre*, and *Tcof1*$^{flx/+}$;*Wnt1-Cre* mice. *Wnt1-Cre* was maintained as a heterozygous allele. To generate *Polr1a*$^{flx/+}$;*Wnt1-Cre*;*RosaeYFP*, *Polr1c*$^{flx/+}$;*Wnt1-Cre*;*RosaeYFP*, and *Tcof1*$^{flx/+}$;*Wnt1-Cre*;*RosaeYFP* mouse lines used for lineage tracing, *Polr1a*$^{flx/+}$;*Wnt1-Cre*, *Polr1c*$^{flx/+}$;*Wnt1-Cre*, and *Tcof1*$^{flx/+}$;*Wnt1-Cre* mice were crossed to *RosaeYFP* (B6.129X1-*Gt(ROSA)26Sor*$^{tm1(EYFP)Cos}$/J, Jax Stock #006148) transgenic mice. *Polr1a*$^{flx/+}$;*Wnt1-Cre*, *Polr1c*$^{flx/+}$;*Wnt1-Cre*, and *Tcof1*$^{flx/+}$;*Wnt1-Cre* males were crossed to *Polr1a*$^{flx/flx}$, *Polr1c*$^{flx/flx}$, and *Tcof1*$^{flx/flx}$ females, respectively to obtain *Polr1a*$^{flx/flx}$;*Wnt1-Cre*, *Porl1c*$^{flx/flx}$;*Wnt1-Cre*, and *Tcof1*$^{flx/flx}$;*Wnt1-Cre* embryos, respectively, which are referred to as *Polr1a*$^{NKO/NKO}$, *Polr1c*$^{NKO/NKO}$, and *Tcof1*$^{NKO/NKO}$ in this paper.

Tamoxifen inducible temporal knockouts

Cre-ER^{T2} (B6.129 – *Gt(ROSA)26Sor*$^{TM1(Cre–ERT2)Tyj}$/J, Jax stock cat# 008463) mice were crossed to *Polr1a*$^{flx/flx}$, *Polr1c*$^{flx/flx}$, and *Tcof1*$^{flx/flx}$ mice to generate *Polr1a*$^{flx/+}$;*Cre-ER*^{T2}, *Polr1c*$^{flx/+}$;*Cre-ER*^{T2}, and *Tcof1*^{flx}/+;*Cre-ER*^{T2} mice which were subsequently bred to homozygous floxed mice to generate embryos for MEF generation.

The day a vaginal plug was observed in a time mated female was designated as embryonic day (E) 0.5. All mice were housed in a 16 hour light: 8 hour dark light cycle. All animal experiments were conducted in accordance with Stowers Institute for Medical Research Institutional Animal Care and Use Committee approved protocol (IACUC #2019-097).

Genotyping

To confirm recombination, *Polr1a* and *Tcof1* mice were genotyped according to the primers listed in Supplemental Table 2. Genotyping of all mouse strains was determined using real-time PCR assays with specific Taqman probes designed for each strain (Transnetyx, Inc, Cordova, TN)

Brightfield imaging

Embryos were imaged on a Leica MZ16 microscope equipped with a Nikon DS-Ri1 camera and NIS Elements imaging software. Manual Z stacks were taken and then assembled using Helicon Focus software. Alterations of brightness and contrast were performed in Adobe Photoshop to improve image clarity and applied equally across the entire image.

MudPIT

A stable cell line expressing FLAG-tagged mouse Treacle was generated by transfecting 293-FRT cells with FLAG-Tcof1-pcDNA5/FRT and pOG44 (Invitrogen) using LipofectAMINE 2000(7). Cells were cultured at 37°C in a humidified incubator with 5% CO_2. Cells were lysed in lysis buffer (50 mM Tris-HCl (pH 7.5), 120 mM NaCl, 0.5% NP-40, 1 mM EDTA, and proteinase inhibitor cocktail (Nacalai tasque)). Following lysis, 2 mM $MgCl_2$ and benzonase (50 U/ ml) was added to the whole cell extracts and centrifuged. The supernatant was incubated with agarose beads conjugated with anti-FLAG antibody (Sigma) at 4°C overnight. The following day, the beads were precipitated by centrifugation, washed with lysis buffer, and proteins were eluted with the FLAG peptide (200 µg/ml) in lysis buffer and then precipitated by Trichloroacetic acid. MudPIT was performed to identify interacting proteins as described previously (8, 9).

Bone and cartilage staining

E18.5 embryos were anesthetized by immersion in ice cold PBS for at least 60 minutes until no reflex movements were observed following a pinch test. The skin and viscera were removed, and the embryos were then fixed in 95-100% ethanol overnight at room temperature or longer at 4°C. Embryos were then stained for bone and cartilage with Alizarin red and Alcian blue, respectively, as previously described (10). The stained embryos were imaged in 50% glycerol with an MZ16 microscope as described above. Skull measurements were made from the occipital to the nasal bone and mandible measurements were made from the condylar process to the base of the incisor. Measurements of the skull and mandible were taken using ImageJ (NIH, Bethesda, MD).

BMH-21 treatment

E8.5 embryos were dissected with an intact yolk sac in Tyrode's buffer and cultured in pre-heated complete media containing 50% DMEM-F12, 50% rat serum, and 1X penicillin/streptomycin in roller culture bottles with 5%CO_2, 5% O_2, and 90% N_2 (7, 11). After 60 minutes of equilibration, 1 µM of BMH-21 (Sigma Aldrich, #SML1183) was added to disrupt Pol I activity. Following 8 hours of incubation, embryos were fixed in 4% PFA/PBS at 4°C overnight. Embryos were stained with Sox2 (1:500, R&D Systems, #AF2018) and Sox10 (1:1000, Abcam, # ab155279) antibodies as well as DAPI following procedures described below. TUNEL assay was performed following manufacturer's protocol (Roche) described below. The stained embryos were sectioned at 10 µm thickness and imaged using a Zeiss LSM 700 confocal microscope. The sectioned images (three biological replicates and two technical replicates) were analyzed using ImageJ (NIH, Bethesda, MD). Sox2 and Sox10 positive cells were grouped as neuroepithelium and neural crest cells and all other cells were grouped as non-neural crest cells.

View RNA and in-situ hybridization

E9.5 and 10.5 embryos were harvested in 1X PBS/0.1% DEPC and fixed in 4% PFA in 1X PBS/0.1% DEPC overnight at 4°C. *In situ* hybridization for *Col2a1* (plasmid obtained from Dr. Ralph Marcucio) was performed using standard protocols as previously described (12). Control and mutant embryos were imaged at the same magnification on a Leica stereoscope using a Nikon DS-Ri1 camera. For ViewRNA, embryos were cryosectioned in RNAse free conditions at a thickness of 10µm. Sections were air dried for 20 minutes and washed with 1X PBS. Sections were then dehydrated in 100% ethanol for 5 minutes followed by antigen retrieval with pre-made target retrieval solution (RNAscope® Cat. No. 320850) or citric acid buffer pH 6 (0.1M sodium citrate, 0.1M citric acid in water) at 95°C for 12 minutes. Following proteinase treatment for 5 minutes at room temperature, sections were hybridized and stained per ViewRNA manual instructions (Invitrogen Catalog number: 88-19000) with custom probes (ThermoFisher, #VPXGPXC, Lot no. 308431918).

Quantification

Embryo sections were imaged with an LSM-700 upright confocal laser scanning microscope. Prior to intensity quantification, Z stacks of mouse embryo sections stained with antibodies or RNA FISH were sum projected and a uniform background was subtracted based on a manually selected region near the neural tube. Nuclei were detected based on the DAPI signal using a two-dimensional version of the algorithm used for the Click-IT OPP analysis above. Analysis was performed with the aid of the PyImageJ (https://github.com/imagej/pyimagej) interface to Fiji (13) from Jupyter Notebooks (https://jupyter.org/) which is available in the Stowers Original Data Repository. For detection, mask diameters were 20 pixels with a threshold of 20% of the maximum intensity as before. Average intensity measurements

were performed using the same mask diameter and two-dimensional histograms and measurements were made of YFP signal vs. ViewRNA signal.

OPP assay

E8.5 and E9.5 *Wnt1Cre;YFP* embryos were cultured in 1:1000 OPP in DMEM-F12 culture media for 1 hour, followed by the Click-IT reaction per Click-iT™ Plus OPP Protein Synthesis Assay Kit (Invitrogen, Catalog #C10457) manual instructions. MEFs treated with tamoxifen and DMSO were treated with 1:500 OPP for 3 hours, followed by the Click-IT reaction.

Quantification

Embryos were imaged with an LSM-700 upright confocal laser scanning microscope. OPP intensity levels were quantified using custom ImageJ (NIH, Bethesda, MD) plugins (13). Detection of nuclear positions from the DAPI signal was performed using a maximum mask approach. This method detects the maximum intensity in the 3D image and then masks out a spheroidal region around it with an XY diameter of 25 pixels and z diameter of 15 slices. The maximum intensity is then found again and masked again repeatedly until there are no maximum pixels above a specified threshold. The threshold was set as 20% of the maximum DAPI intensity in the image. This algorithm does not find the nuclear positions perfectly, but it does provide a measurement proportional to the nuclear density. Average intensities in the YFP and OPP channels were then measured centered at the nuclear positions in a spheroid with an XY diameter of 20 pixels and a z diameter of 10 slices. This smaller measurement region ensures that slightly overlapping nuclei do not significantly influence the measurement. Two dimensional logarithmically binned histograms were made of the YFP signal (denoting the neural crest population) vs. the OPP signal. Those histograms showed clear positive and negative YFP populations allowing for manual drawing of rectangular gates for these populations followed by simple average intensity per cell calculations. In some cases, laser powers were adjusted during the signal acquisition and those values were corrected for in the measurement of the intensities.

β-galactosidase staining

E8.0-E9.5 embryos were collected and fixed in 2% PFA/0.2% glutaraldehyde in PBS for the following time durations: E8.5-E9.0 for 15 minutes and E9.5 for 30-45 minutes at 4°C. Embryos were rinsed with PBS and stained according to manufacturer's protocol (Millipore #BG-6-B, #BG-7-B, #BG-8-C). Embryos were then fixed again in 4%PFA/PBS at 4°C rocking overnight and washed in PBS for whole embryo brightfield imaging. For sections, embryos were rinsed and immersed into 30% sucrose/PBS overnight at 4°C. The following day they were submerged into 1:1 30% sucrose/OCT

and then embedded in OCT and cryosectioned at a thickness of 10µm. Sections were then imaged on an Axioplan 206 Std microscope with Micro-manager 1.4, Win 10 software.

Immunostaining

Embryos were harvested at the desired developmental stages in 1X PBS and fixed in 4% PFA/1X PBS at 4°C overnight with the exception of p53 staining which required fixation in 4% PFA/1X PBS at 4°C for 3 hours. For whole embryo staining, the embryos were dehydrated through an ascending methanol series into 100% methanol and stored in -20°C overnight. Next, embryos were treated with 4:1:1 Methanol: DMSO: Hydrogen Peroxide and rehydrated through a descending methanol series into PBS. Embryos were blocked with 2% BSA/2% goat serum prior to staining. For section-staining, the fixed embryos were cryosectioned transversely at 10 µm thickness, followed by blocking solution and staining as previously mentioned. For p53 staining, antigen retrieval was performed by immersing the sections in pre-warmed citric acid buffer (pH6, 0.1M sodium citrate, 0.1M citric acid in water) and incubated at 80-90°C for 30 minutes. Sections were then permeabilized with 0.5% TritonX-100 in PBS followed by 3% BSA blocking solution. Primary antibodies used were: Tcof1 (1:1000, Abcam# ab65212), Sox9 (1:200, Abcam # ab185966), TuJ1 (1:500, Covance Research products, # MMS-435P), GFP (1:500, Life Technologies #A6455), phospho-histone H3 (1:2000, Millipore # 06-570), p53 (1:100, Cell Signaling Technology #2524S), γ-H2AX (1:400, Cell Signaling Technology #2577) and Y10b (1:1000, Abcam #ab171119). The embryos and sections were counter-stained with DAPI (Sigma-Aldrich #D9564) to visualize the nuclei. Embryos were imaged with an LSM-700 upright confocal laser scanning microscope. Confocal optical slices were collected and maximum-intensity projections of stacks were made with Zeiss LSM software. Figures were assembled in Adobe Photoshop with adjustments of brightness applied uniformly across images to improve visualization.

Quantification

pHH3 measurements were performed similarly to the ViewRNA measurements. The DAPI channel was Gaussian blurred with a standard deviation of 5 pixels and the diameter for nuclear detection was 45 pixels with a threshold at 15% of the maximum intensity. The measurement diameter was 30 pixels. By averaging the intensity of four brightest cells in the image, our quantification method assumes that there are at least 4 positive cells in each image which we have confirmed by visual inspection. The cutoff for positive cells was then set at 20% of that positive value and the fraction of cells above that cutoff was measured. Measurements are only reported for the YFP positive population. p53 measurements were performed identically to pHH3 but including all cells in the section. For statistical analysis, fluorescence intensities of $Polr1a^{NKO/NKO}$, $Polr1c^{NKO/NKO}$, and $Tcof1^{NKO/NKO}$ were compared to $Polr1a^{NKO/+}$, $Polr1c^{NKO/+}$, and $Tcof1^{NKO/+}$, respectively.

TUNEL staining

Following overnight 4% PFA/PBS fixation, embryos were washed in 1X PBS and then dehydrated through an ascending methanol series into 100% methanol and stored at -20°C overnight for wholemount staining. Embryos were then rehydrated through a descending methanol series into PBS. Alternatively, after fixation, embryos were placed into 30% sucrose/PBS overnight at 4°C and then embedded in OCT for cryosectioning. Embryos and cryosections were permeabilized in 0.1% sodium citrate/PBT (0.1% TritonX in 1X PBS) for 10 minutes at room temperature. Samples were then washed in PBS and incubated with 1:19 TUNEL enzyme: buffer (Roche) at 37°C in the dark for 1-2 hours and then counter-stained with DAPI (Sigma-Aldrich #D9564). Embryos were imaged with an LSM-700 upright confocal laser scanning microscope similar to the immunostaining.

Quantification

TUNEL measurements were performed similarly to the ViewRNA measurements. The fraction of positive cells was measured as the fraction of cells with an intensity above 10,000 units, a level corresponding approximately to the level of positive cells seen in the image. Measurements are reported only for the YFP+ population.

BrdU labelling

To analyze cell proliferation, E8.5 pregnant mice were injected intraperitoneally with BrdU at 0.1mg/kg of body weight. After 30 minutes of incubation, mice were sacrificed. For detection of BrdU-positive cells, transverse cryosections were incubated with 1M HCl for 30 minutes at 37°C after immunostaining with pHH3 (Millipore # 06-570, dilution 1:500), and following secondary antibody incubation. BrdU-positive cells were detected by immunostaining using a rat anti-BrdU antibody (Abcam, dilution 1:200). The number of BrdU+ and pHH3+ cells in neuroepithelium, mesoderm and endoderm were counted (three biological replicates, five technical replicates). Fluorescence microscopy was performed on a LSM5 PASCAL confocal microscope (Carl Zeiss).

Cell sorting

E9.5 and E10.5 embryos were dissected in Tyrode's buffer and yolk sacs were saved for genotyping. Control and mutant embryos positive for YFP were used for the cell sorting. The embryos were incubated at 37°C for 5 minutes with TypLE (Gibco) and vortexed for 10 seconds. This cycle of incubation and vortexing was repeated for a period of 15-20 minutes to obtain a single cell suspension, following which TypLE was quenched with fetal bovine serum. The cells were then centrifuged at 200 rcf for 10 minutes. The supernatant was discarded, and the cells were resuspended in PBS. 1μl of 100 μg/ml propidium iodide was added to gate viable cells and the cells were sorted using a FACSMelody (BD Biosciences). YFP+ and YFP- live cells were immediately processed for RNA and protein isolation (2000 cells each). Downstream analysis was performed after confirmation of genotypes.

RNA isolation, cDNA preparation and qPCR

RNA was extracted from sorted YFP+ and YFP- cells from control and mutant embryos using the Qiagen miRNeasy Micro Kit with on-column DNase treatment. RNA was tested for quality on the Agilent 2100 Bioanalyzer and only RNA samples with a RIN score greater than 8.0 were used. The Superscript III Kit (Invitrogen) was used to synthesize cDNA for quantitative RT-PCR (qPCR) using random hexamer primers. qPCR was performed on ABI7000 (Thermo QuantStudio 7) using Perfecta Sybr Green (Quantbio # 95072-250). Primers are listed in Supplemental Table 2. Primers for *Polr1a* were designed on exons upstream of the floxed exon while primers for *Polr1c* and *Tcof1* were designed on the floxed exon. No template controls were run as negative controls. $\Delta\Delta C_t$ method was used to calculate fold change. Student's t-test and ANOVA were used for statistical analysis and significance was determined based on $p < 0.05$.

Silver staining

2000 YFP+ cells and YFP- cells from controls and mutants were sorted using a FACSMelody (BD Biosciences) sorter as mentioned previously. Cells were lysed at 4°C for 30 minutes using 20 µl of lysis buffer containing Tris pH 8.0, sodium chloride, sodium deoxycholate, SDS, NP-40, and protease inhibitor. Following lysis, the cells were centrifuged at 13,000 rpm at 4°C for 30 minutes. 1X Laemmli buffer (loading buffer) was added to the extracted protein and denatured at 95°C for 5 minutes. The protein was then loaded onto 4-20% gradient SDS-PAGE gels and run in an electrophoresis unit for 90 minutes at 90V. The gel was then stained using a Pierce Silver Stain kit (ThermoFisher Scientific, #24612) following the manufacturer's instructions. Band intensities were measured as area under the curve using ImageJ.

Mouse embryonic fibroblast derivation

Mouse embryonic fibroblast cells (MEFs) were derived from E13.5 and E14.5 *Polr1a$^{flx/flx}$, Polr1a$^{flx/flx}$;Cre-ER^{T2}, Polr1c$^{flx/flx}$, Polr1c$^{flx/flx}$;Cre-ER^{T2}, Tcof1$^{flx/flx}$* and *Tcof1$^{flx/flx}$;Cre-ER^{T2}* embryos as described previously (14). Cells were cultured in a complete media containing DMEM, 30% FBS, 1X L-Glutamine, 1X Non-essential amino acids, and 1X 2-mercaptoethanol and kept in passage for 3-5 generations. For deletion of *Polr1a*, *Polr1a$^{flx/flx}$;Cre-ER^{T2}* MEFs were treated with 5 µM tamoxifen dissolved in DMSO, while *Polr1c* and *Tcof1* deletion was performed by treating *Polr1c$^{flx/flx}$;Cre-ER^{T2}* and *Tcof1$^{flx/flx}$;Cre-ER^{T2}* MEFs with 1µM tamoxifen. *Polr1a$^{flx/flx}$, Polr1c$^{flx/flx}$* and *Tcof1$^{flx/flx}$* MEFs treated with tamoxifen were used as controls. The treatment was performed for 24 hours and the cells were allowed to recover for 24 hours. All experiments were performed 48 hours post tamoxifen induction with three biological replicates of MEFs derived from three mutants as

well as in three technical replicates. RNA isolation and qPCR were performed using the same approach and primers as above.

Western blot

MEFs treated with tamoxifen were lysed using lysis buffer and western blot was performed using standard protocols as described previously (15). Protein quantity was estimated via a BCA assay. Antibodies used were p53 (1:500, Cell Signaling Technology, #2524S), Rpl5 (1:1000, Cell Signaling Technology, #51345), Rpl11 (1:1000, Cell Signaling Technology, #18163), Mdm2 (1:500, Cell Signaling Technology, #86934) and γ-Tubulin (1:1500, Millipore Sigma, #T6557). Western blots were imaged and quantified using a CLx-Scanner (Li-COR) and Odyssey Software. For quantification, band intensities for Rpl5, Rpl11, Mdm2 and p53 were compared to housekeeping control γ-Tubulin. Student's t-test was performed for statistical analysis.

Immunoprecipitation

MEFs were cultured on a T75 plate and harvested following tamoxifen treatment. Immunoprecipitation was performed as previously described (15). Briefly, the cells were homogenized in 500 µl lysis buffer containing Tris pH 8.0, Sodium Chloride, SDS, Sodium deoxycholate, NP-40 and protease inhibitor. The homogenized mixture was then incubated with overhead rotation for 30 minutes at 4°C followed by centrifugation at 13,000 rpm at 4°C. The lysate was then divided into two tubes with of equal protein content, one for incubation with Normal Rabbit IgG and the other for incubation with Mdm2 antibody (Cell Signaling Technology, #86934). 2 µg of antibody was used per mg of protein for immunoprecipitation. 10% volume of the lysate used for immunoprecipitation was collected separately to be used for the control input lane for western blot analysis. The lysate-antibody mix was incubated at 4°C overnight with overhead rotation with a speed of 40 rpm. The following day pre-washed Dynabeads were incubated with the lysate-antibody mix at 4°C for 4 hours. The beads were then washed and eluted with 2X Laemmli buffer at 95°C. The eluted protein was then used for SDS-PAGE and western blot. The protein bands were detected using antibodies against p53 (Cell Signaling Technology, #2524S), Rpl5 (Cell Signaling Technology, #51345), Rpl11 (Cell Signaling Technology, #18163) and Mdm2 (Cell Signaling Technology, #86934). For each biological replicate, cells from one T75 culture plate were used for immunoprecipitation. The experiment was performed in three biological and three technical replicates. For quantification, band intensity of Rpl5, Rpl11, and p53 were compared to Mdm2 in both control and mutant cells. Student's t-test was performed for statistical analysis.

Drug Treatment

Pregnant dams were injected intraperitoneally for four consecutive days from E6.5-E9.5 with 3 mg of pifithrin-α per kg of body weight of the mouse. For control experiments, pregnant mice were injected with 200 ul of 50% DMSO for the same period of time. At E10.5, the embryos were dissected and immunostained with an antibody against GFP to detect the YFP+ neural crest cell population.

Single cell RNA sequencing

Tissue collection

6 *Mef2c-F10N-LacZ* (4) and 6 *Wnt1-Cre;RosaeYFP* (6, 16, 17) mice were collected at E8.5. Cranial tissues were manually dissected and incubated in 0.25% Trypsin+EDTA in a 37°C water bath for 1 minute and dissociated through gentle repetitive pipetting about 10 times. The tube was then incubated again in a 37°C water bath for another minute prior to the addition of cold FBS to quench Trypsin activity. Samples were then centrifuged at 1600 rcf at 4°C for 15 minutes. The supernatant was discarded and the cells were resuspended in 200 μl PBS+2% FBS. Cells were centrifuged again and resuspended in 40 μl PBS. Genotyping was performed after cell dissociation which indicated that 3 out of the 6 *Mef2c-F10N-LacZ* embryos were LacZ positive and that 4 out of the 6 *Wnt1-Cre;RosaeYFP* embryos were YFP positive.

Processing and Sequencing

Dissociated cells were assessed for concentration and viability using a Luna-FL cell counter (Logos Biosystems). The cells were confirmed to have at least 70% viability and 12,000-15,000 cells per sample were loaded on a Chromium Single Cell Controller (10x Genomics). Libraries were prepared using the Chromium Next GEM Single Cell 3' Library & Gel Bead Kit v3.1 (10x Genomics) according to manufacturer's directions. Resulting short fragment libraries were checked for quality and quantity using a Bioanalyzer (Agilent) and Qubit Fluorometer (ThermoFisher). Libraries were pooled at equal molar concentrations and sequenced on an Illumina NovaSeq 6000 S1 flow cell with the following paired read lengths: 28 bp Read1, 8 bp I7 Index and 98 bp Read2.

Data processing

Raw sequencing data was processed using Cell Ranger (v3.0.0, 10x Genomics) to generate gene-level counts for each cell in each sample. Genes with counts in less than three cells were removed from the dataset. Mitochondrial percentages and feature count distribution were used as criteria for cell quality control. The percent mitochondria threshold was set to keep 75% of cells of the *Mef2c-F10N-LacZ* sample (mito ≤ 10.93%). The same threshold was applied to the *Wnt1-Cre;RosaeYFP* sample, keeping 86% of the cells. In addition, cells with feature counts of > 10,000 or < 500 were also excluded from the analysis. The final dataset used for analysis consisted of 21,190 cells (12,498 cells for *Wnt1-Cre;RosaeYFP* and 8,692 for *Mef2c-F10N-LacZ*) and 29,041 genes and is available at the Gene Expression Omnibus (accession no. GSE168351).

The Seurat package (v3.1.1)(18) was used to normalize data via the SCTransform method (19). Mitochondrial percentage was regressed out during normalization. For clustering, 3000 highly variable genes were selected, and the first 46 principal components based on those genes were used to identify 7 clusters at a resolution of 0.05 using the shared nearest neighbor method. The identities of clusters were determined by the differential gene expression of classic markers for each tissue type. Neuroepithelial cells were identified by high expression of classic markers, *Sox2* and *Sox1*. Neural crest cell reporters, *LacZ* and *pEYFP*, and *Sox10* were used to cluster NCC. Embryonic blood cells were clustered based on *Hba*-x expression and endothelial cells based on *Kdr* expression. *Cdh1* expression was used to identify non-neural ectoderm and *Tbx1* expression was used to cluster endodermal and mesodermal cells. Data was visualized in reduced dimensionality using UMAP.

The expression value for each gene was standardized by subtracting the gene's mean expression and dividing by its standard deviation. For instance, a value of -1 would imply that the value is one standard deviation below the mean expression for that specific gene.
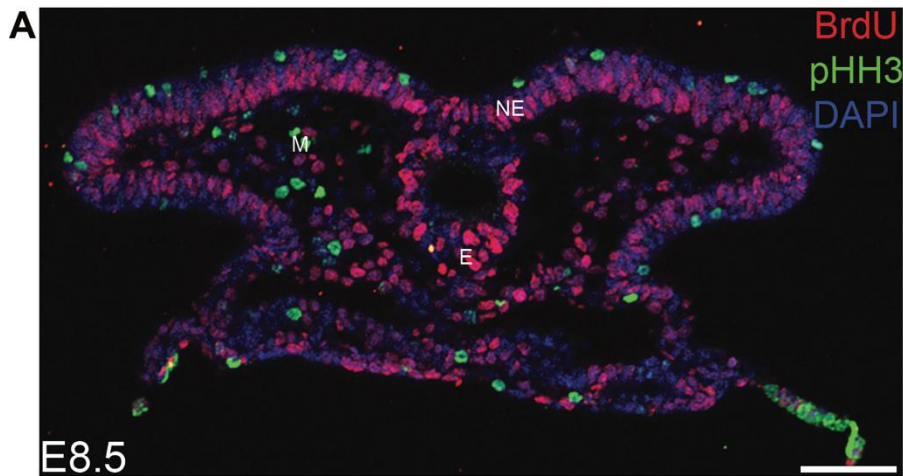
Fig. S1. The neuroepithelium is highly proliferative. (A) A higher number of cells in the neuroepithelium, which includes premigratory NCC, are pHH3 and BrdU positive compared to surrounding mesoderm and endoderm cells, indicating that the neuroepithelium is more highly proliferative at E8.5 in wild-type embryos. (B) Quantification of pHH3 and BrdU positive cells in E8.5 craniofacial tissue from three biological replicates and five technical replicates. Scale bar = 80 μm. Abbreviations: NE, neuroepithelium; M, Mesoderm; E, Ectoderm.
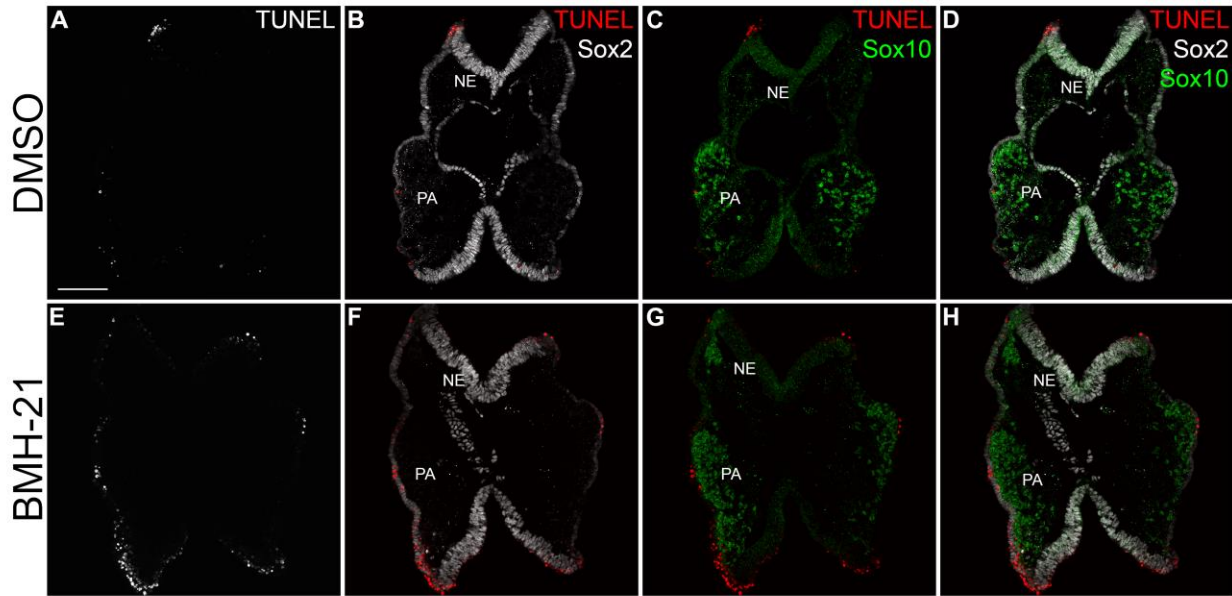
Fig. S2. Inhibition of Pol I transcription leads to higher apoptosis in the neuroepithelium and NCC. Transverse sections of DMSO (A-D) and BMH-21(E-F) treated embryos at E8.5 stained for TUNEL (white in A and E, red in B-D and F-H), Sox2 (white in B-D and F-H) and Sox10 (green in C, D, G and H) show that chemical inhibition of Pol I leads to apoptosis, especially in Sox2 positive neuroepithelium and Sox10 positive NCC. Abbreviations: NE, neuroepithelium; PA, pharyngeal arches. Scale bar = 120 µm.
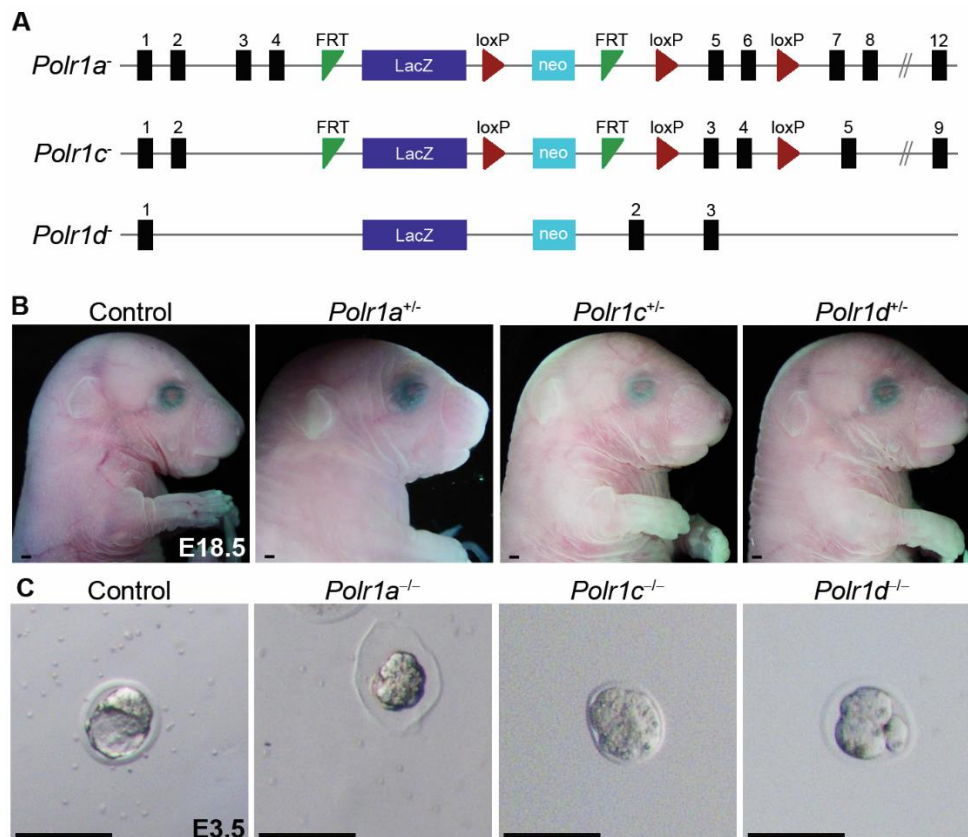
Fig. S3. Generation of *Polr1a, Polr1c* and *Polr1d* mutant mice. (A) A LacZ-neo cassette containing loxP sites flanking critical exons of *Polr1a* and *Polr1c* was used to generate *Polr1a⁺ᐟ⁻* and *Polr1c⁺ᐟ⁻* alleles. The *Polr1d⁺ᐟ⁻* allele was generated by disrupting the *Polr1d* gene with a LacZ-neo insert. (B) Heterozygous mutants of *Polr1a*, *Polr1c* and *Polr1d* are indistinguishable from wild-type controls indicating a single copy of *Polr1a*, *Polr1c* and *Polr1d* is sufficient for embryonic development. Scale bar = 500 μm (C) Null mutants of *Polr1a*, *Polr1c* and *Polr1d* survive until the uncompacted morula stage at E2.5 and are fragmented by E3.5 while wildtype embryos proceed to the blastocyst stage indicating *Polr1a*, *Polr1c* and *Polr1d* are required for pre-implantation embryo survival. Scale bar = 100 μm.
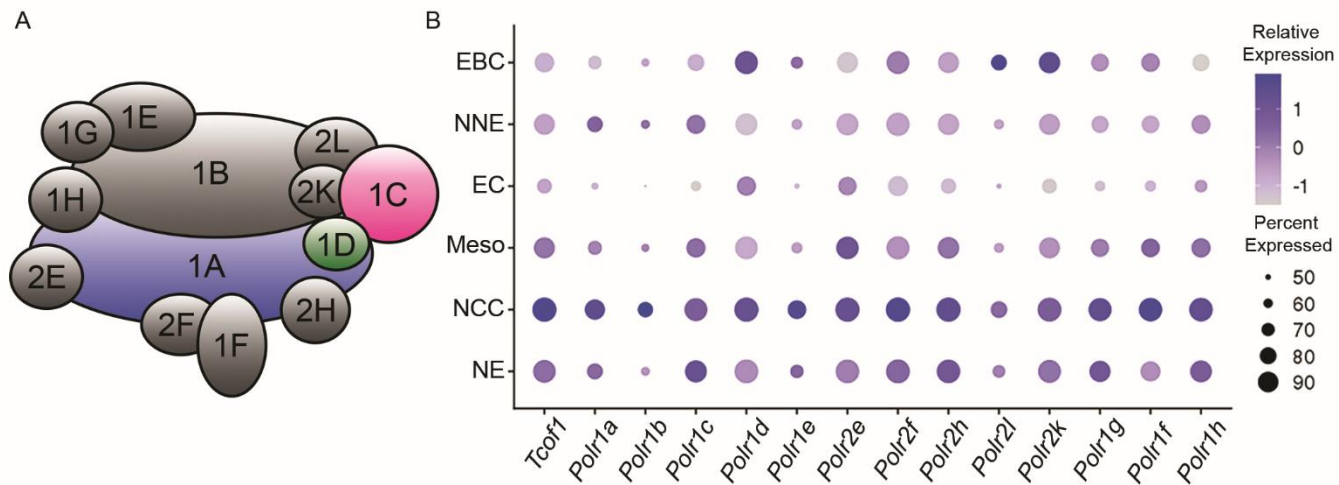
Fig. S4. Pol I subunits are expressed highly in NCC. A) Schematic of RNA Polymerase I subunits. B) Single cell RNA-seq analysis identifies *Tcof1* and RNA Polymerase I subunit transcripts to be highly expressed in neuroepithelium and NCC compared to other tissues in the craniofacial region of E8.5 mouse embryos. The size of the circle represents the percent of cells in a population expressing the transcript of interest, while color intensity represents the relative level of transcripts expressed in a cell population (see Methods). Abbreviations: EBC, embryonic blood cells; EC, endothelial cells; Meso, mesoderm; NCC, neural crest cells; NE, neuroepithelium; NNE, non-neural ectoderm.
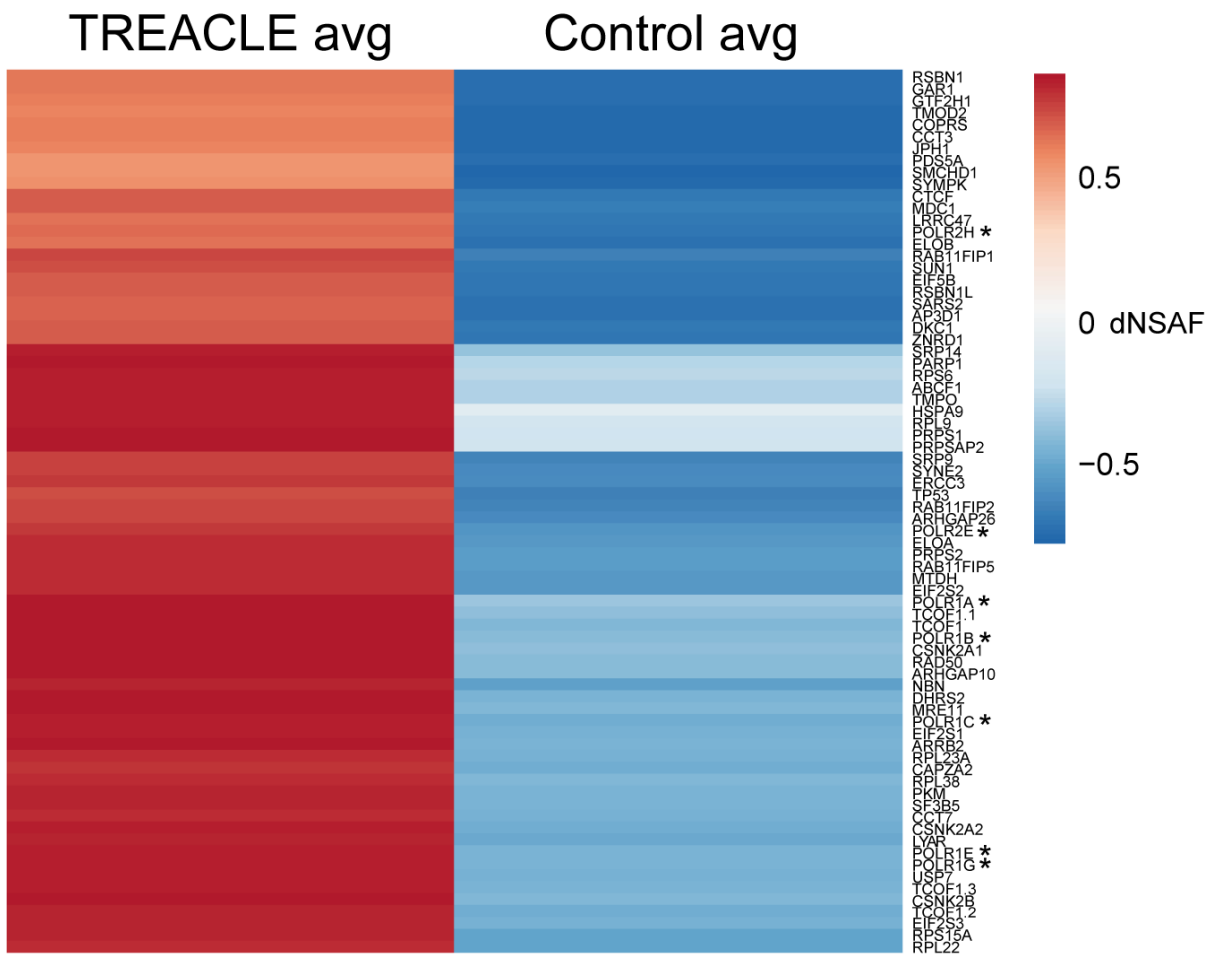
Fig. S5. Proteins identified by multidimensional protein identification technology with Treacle as the bait. Heat map showing the spectral abundance of proteins pulled down with FLAG-tagged Treacle in both antibody and IgG (control) immunoprecipitation conditions, expressed as distributed normalized spectral abundance factor (dNSAF). This demonstrates the specificity of Treacle binding to target proteins. * Pol I protein subunits.
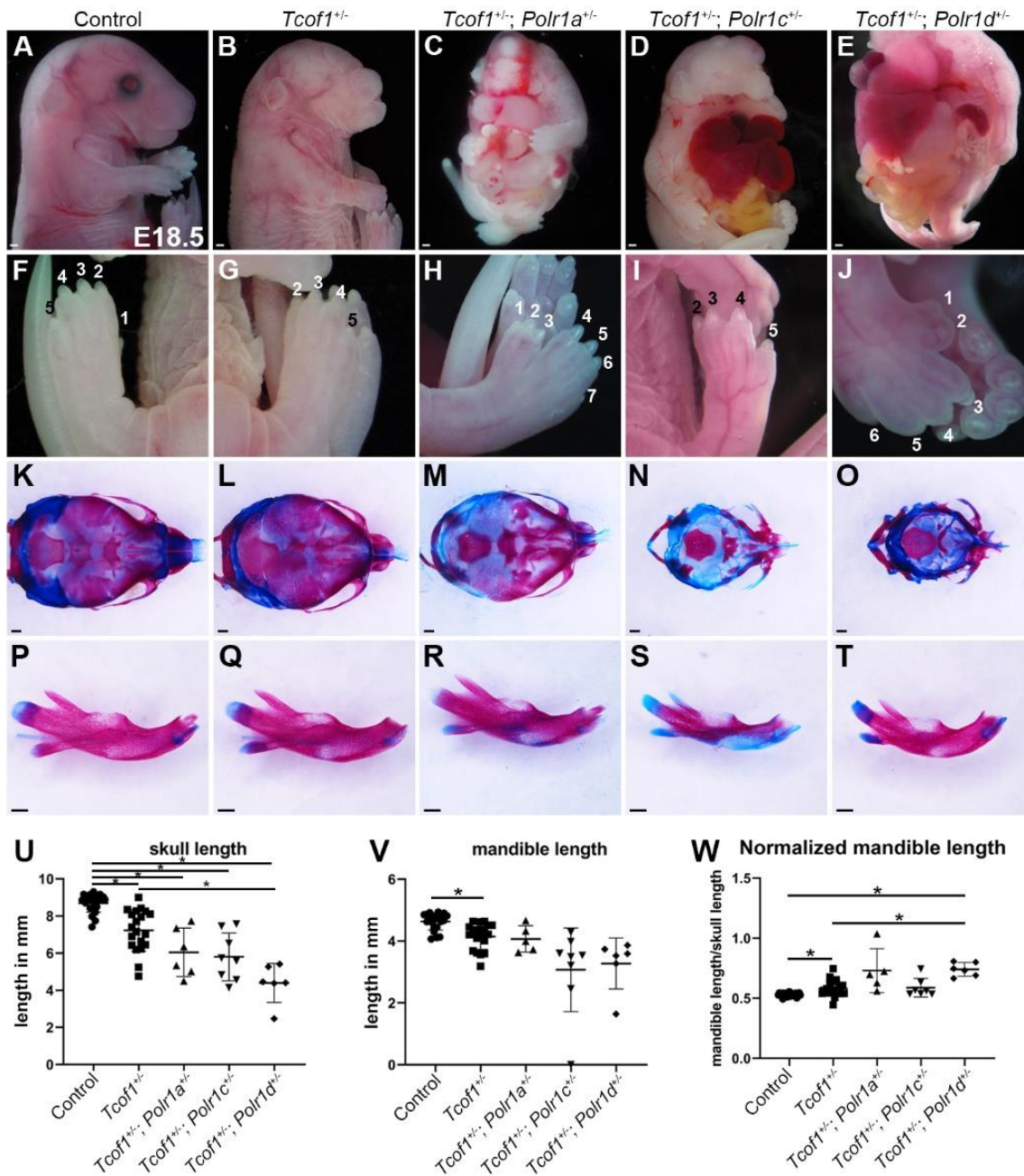
Fig. S6. Double mutants of *Tcof1* with *Polr1a, Polr1c,* and *Polr1d* exhibit thoracoschisis and digit defects. (A-E) Compared to controls and *Tcof1+/-* embryos, *Tcof1+/-; Polr1a+/-, Tcof1+/-; Polr1c+/- and Tcof1+/-; Polr1d+/-* double mutants exhibit variably penetrant thoracoschisis as evidenced by herniation of lung, liver and gut at variable penetrance. (F-J) *Tcof1+/-; Polr1a+/-, Tcof1+/-; Polr1c+/- and Tcof1+/-; Polr1d+/-* double mutants exhibit digit defects including duplication of digit 1 (H,J) and shorter, broader digits (I). (K-O) Alcian blue and Alizarin red stained skeletons reveal hypoplasia of the skull in *Tcof1+/-, Tcof1+/-; Polr1a+/-, Tcof1+/-; Polr1c+/- and Tcof1+/-; Polr1d+/-* mutants, quantified in (U). (P-T) Dissected mandibles from control, *Tcof1+/-, Tcof1+/-; Polr1a+/-, Tcof1+/-; Polr1c+/- and Tcof1+/-; Polr1d+/-* mutants show reduced mandible length, quantified in (V). (W) Quantification of the size of the mandible relative to the skull demonstrates that the proportion of the mandible relative to skull size is variable in mutant mice. * = p<0.05. Scale bar = 500 μm
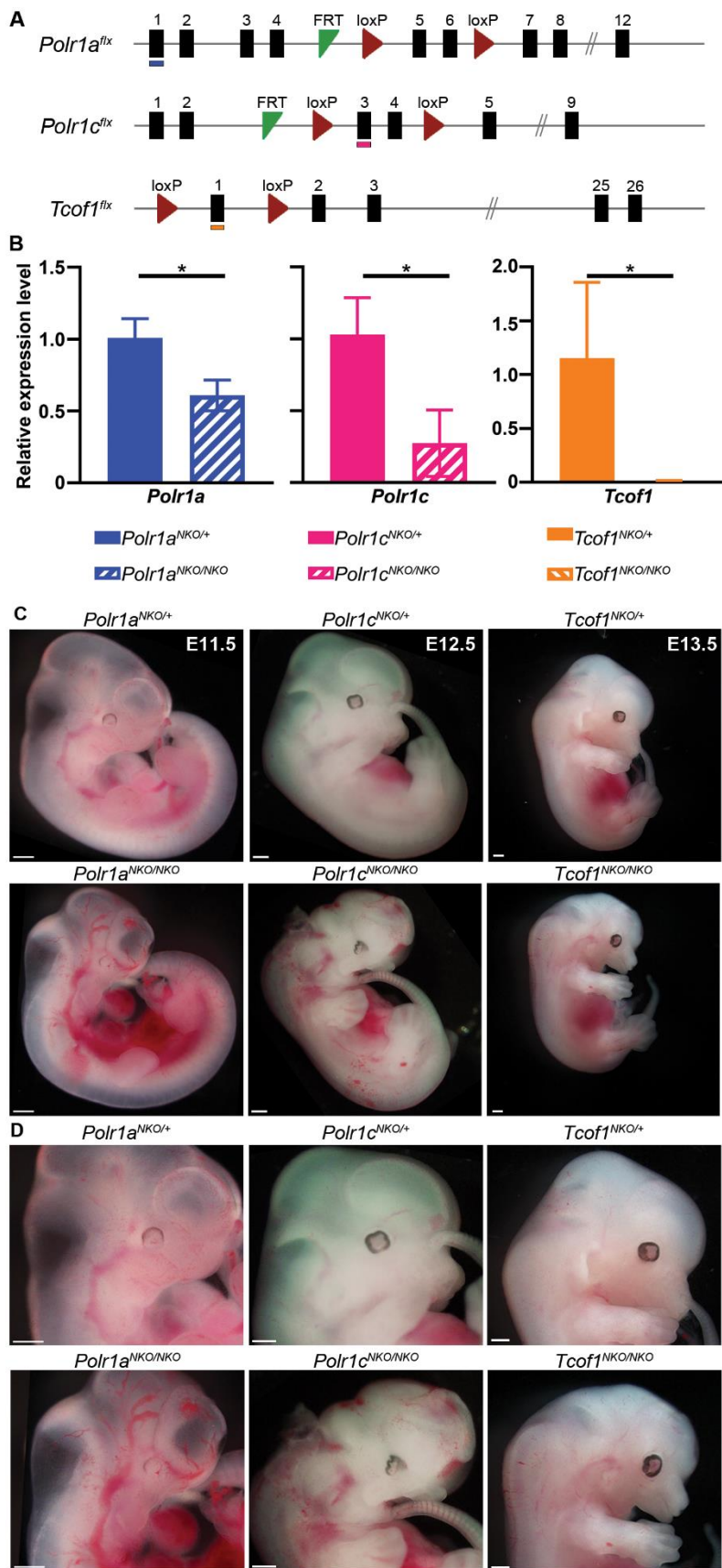
Fig. S7. NCC-specific mutants of _Polr1a_, _Polr1c_ and _Tcof1_ exhibit mid-gestation lethality. (A) NCC-specific knockouts of _Polr1a (Polr1a^NKO), Polr1c (Polr1c^NKO)_ and _Tcof1 (Tcof1^NKO)_ were generated by flanking critical exons with loxP sites and breeding the floxed allelic mice _(Polr1a^flx, Polr1c^flx_ and _Tcof1^flx)_ with _Wnt1-Cre_ transgenic mice. Exons

examined by qPCR in (B) are underlined in each corresponding construct. (B) qPCR reveals reduced expression of *Polr1a*, *Polr1c,* and *Tcof1* transcripts in sorted NCC from *Polr1a$^{NKO/NKO}$*, *Polr1c$^{NKO/NKO}$*, and *Tcof1$^{NKO/NKO}$* embryos, respectively, compared to their control littermates at E9.5. *indicates p<0.05, Student's t-test. (C) While a single copy of *Polr1a*, *Polr1c* and *Tcof1* in NCC is sufficient for embryonic development, knocking out both copies of *Polr1a*, *Polr1c* and *Tcof1* from NCC results in midgestation lethality. (D) Higher magnification images of (C). Scale bar = 500 μm.
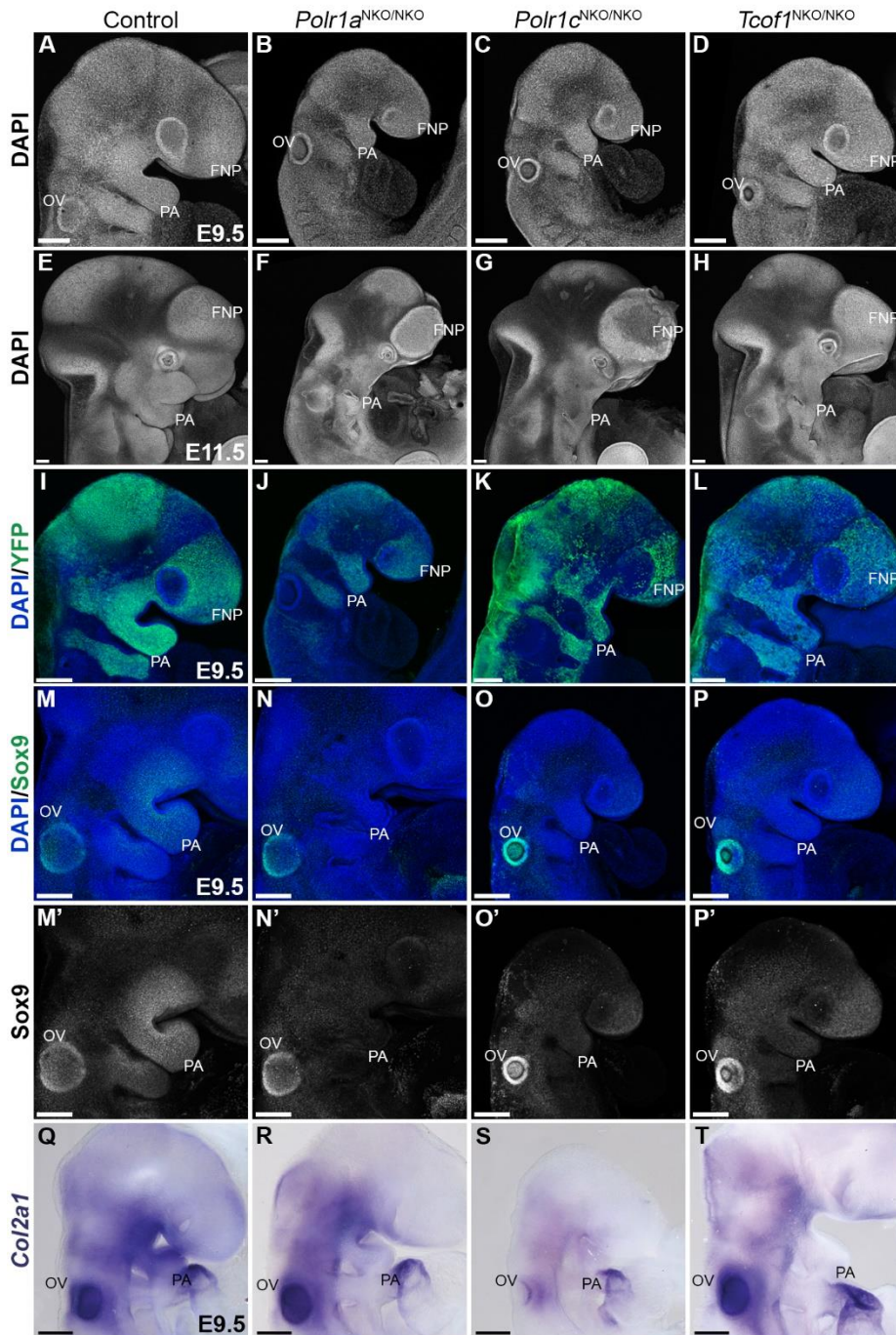
Fig. S8. Craniofacial defects in *Polr1a^NKO/NKO*, *Polr1c^NKO/NKO* and *Tcof1^NKO/NKO* mice. (A-H) DAPI staining of control, *Polr1a^NKO/NKO*, *Polr1c^NKO/NKO* and *Tcof1^NKO/NKO* embryos at E9.5 and E11.5 shows hypoplastic pharyngeal arches and frontonasal prominences in *Polr1a^NKO/NKO*, *Polr1c^NKO/NKO* and *Tcof1^NKO/NKO* embryos. (I-L) Analysis of the NCC lineage with RosaeYFP indicates that fewer NCC migrate to the pharyngeal arches in *Polr1a^NKO/NKO*, *Polr1c^NKO/NKO* and *Tcof1^NKO/NKO* at E9.5. (M-P) Immunostaining for Sox9, a marker indicative of NCC migration and differentiation to chondrocytes (green in M-P and grayscale in M'-P'). Sox9 is significantly reduced in the pharyngeal arches of *Polr1a^NKO/NKO*, *Polr1c^NKO/NKO* and *Tcof1^NKO/NKO* embryos, indicating a reduction in the number of NCC precursors necessary for craniofacial cartilage development. (Q-T) Consistent with this, Type II collagen *Col2a1* transcription is drastically reduced in the pharyngeal arches of *Polr1a^NKO/NKO*, *Polr1c^NKO/NKO* and *Tcof1^NKO/NKO* embryos at E9.5. Abbreviations. FNP, Frontonasal prominence; NE, neuroepithelium; OV, Otic vesicle. PA, pharyngeal arches; Scale bar = 200 μm.
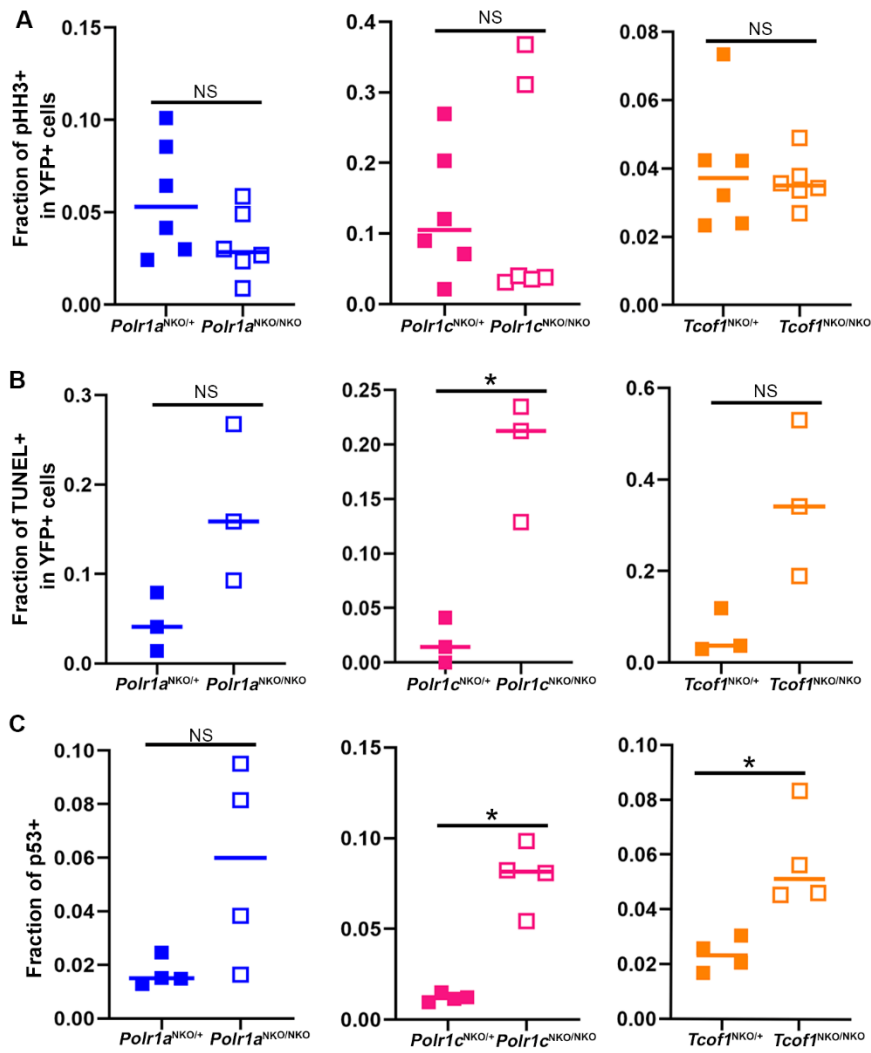
Fig. S9. Quantification of pHH3, TUNEL, and p53 in NCC of *Polr1a^{NKO/NKO}*, *Polr1c^{NKO/NKO}* and *Tcof1^{NKO/NKO}* embryos compared to *Polr1a^{NKO/+}*, *Polr1c^{NKO/+}* and *Tcof1^{NKO/+}* controls. (A) Quantification of pHH3+; YFP+ cells demonstrates that pHH3 staining in the NCC at E9.5 tends to be less in *NKO/NKO* mutants relative to littermate controls, however this difference is not statistically significant. (B) Quantification of TUNEL+;YFP+ cells reveals increased cell death in *NKO/NKO* mutants. This trend is statistically significant in *Polr1c^{NKO/NKO}* embryos. (C) Similarly, quantification of p53+ cells revealed increased levels of p53 in *NKO/NKO* mutants. This trend is statistically significant in *Polr1c^{NKO/NKO}* and *Tcof1^{NKO/NKO}* embryos relative to their littermate controls. * indicates p<0.05, Student's t-test.
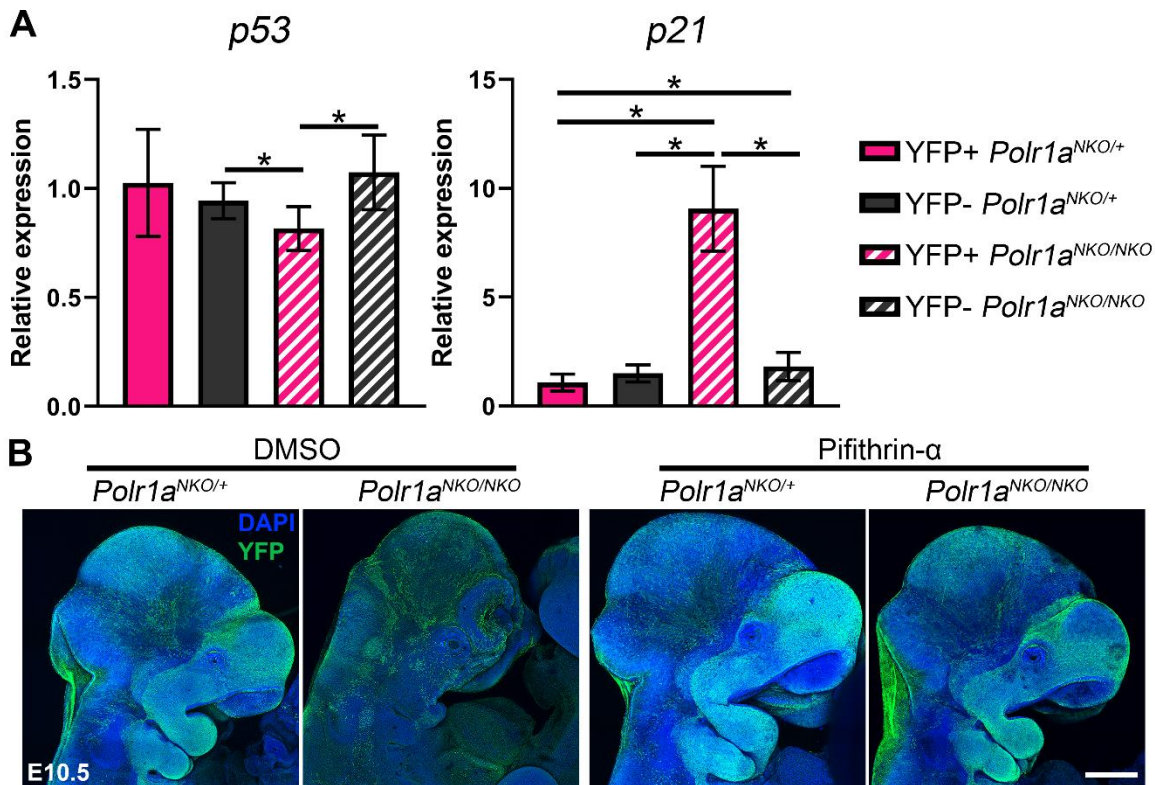
Fig. S10. Quantification of *p53* and *p21* transcript in NCC and non-NCC of *Polr1a^{NKO/NKO}* embryos compared to *Polr1a^{NKO/+}* controls. (A) qPCR for *p53* demonstrates that *p53* levels are not significantly changed in NCC versus non-NCC in control embryos (YFP+ *Polr1a^{NKO/+}* vs. YFP- *Polr1a^{NKO/+}*) while *p53* transcript levels are significantly downregulated in NCC versus non-NCC in mutant embryos (YFP+ *Polr1a^{NKO/NKO}* vs. YFP- *Polr1a^{NKO/NKO}*) and versus non-NCC in controls (YFP+ *Polr1a^{NKO/NKO}* vs. YFP- *Polr1a^{NKO/+}*). However, *p53* levels in the NCC population between YFP+ *Polr1a^{NKO/NKO}* mutants and *YFP+ Polr1a^{NKO/+}* controls was not significantly changed. qPCR for *p21* demonstrates that *p21* is significantly upregulated in YFP+ *Polr1a^{NKO/NKO}* mutants compared to all other cell populations examined. *indicates $p < 0.05$, Welch's ANOVA, Dunnett's T3 multiple comparisons test. (B) Immunostaining for YFP to assess NCC lineage in DMSO and pifithrin-α treated *Polr1a^{NKO/NKO}* and control embryos indicates that pifithrin-α treatment rescues the pharyngeal arch volumes as well as NCC population in *Polr1a^{NKO/NKO}* embryos. Scale bar = 400 µm.
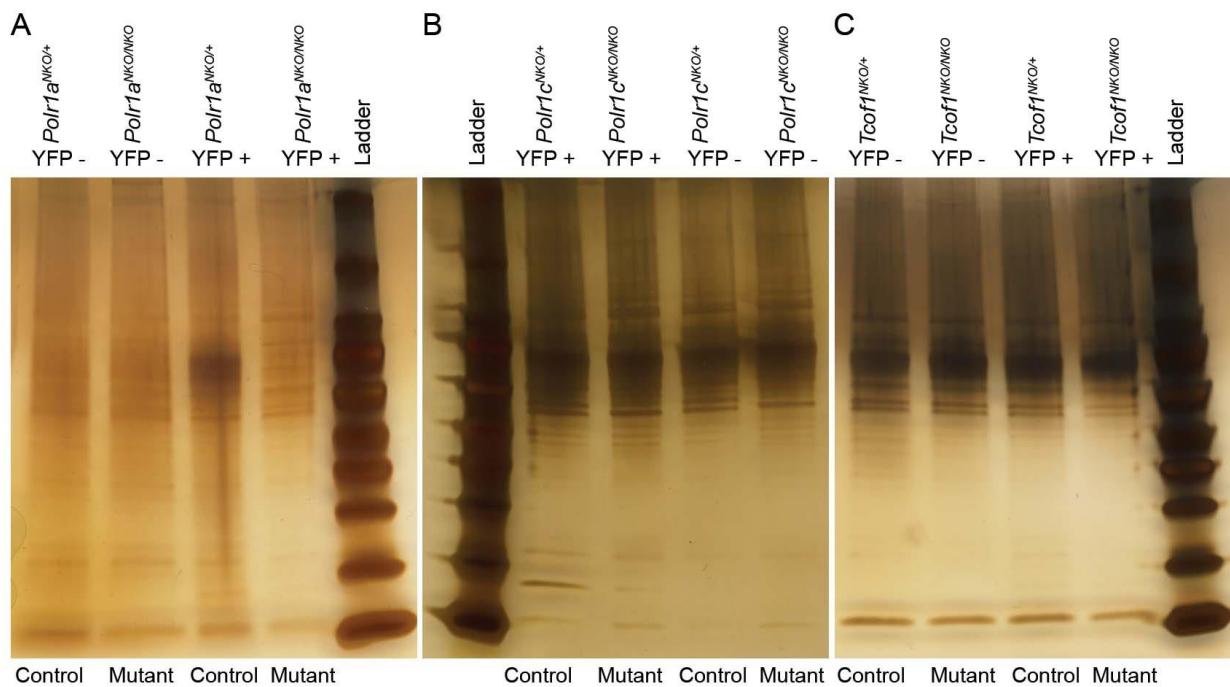
Fig. S11. Total protein is significantly reduced in the NCC of *Polr1a^NKO/NKO*, *Polr1c^NKO/NKO* and *Tcof1^NKO/NKO* mice.

(A-C) Silver staining reveals that total protein levels in equal numbers of NCC (YFP+) is slightly higher compared to non-NCC (YFP-) in E10.5 control embryos as observed by the number of bands and intensity of bands in silver-stained gels. However, protein levels in NCC (YFP+) are comparable to non-NCC (YFP-) in mutant *Polr1a^NKO/NKO*, *Polr1c^NKO/NKO* and *Tcof1^NKO/NKO* embryos. Compared to control NCC (YFP+), protein expression is significantly lower in mutant *Polr1a^NKO/NKO*, *Polr1c^NKO/NKO* and *Tcof1^NKO/NKO* NCC (YFP+).

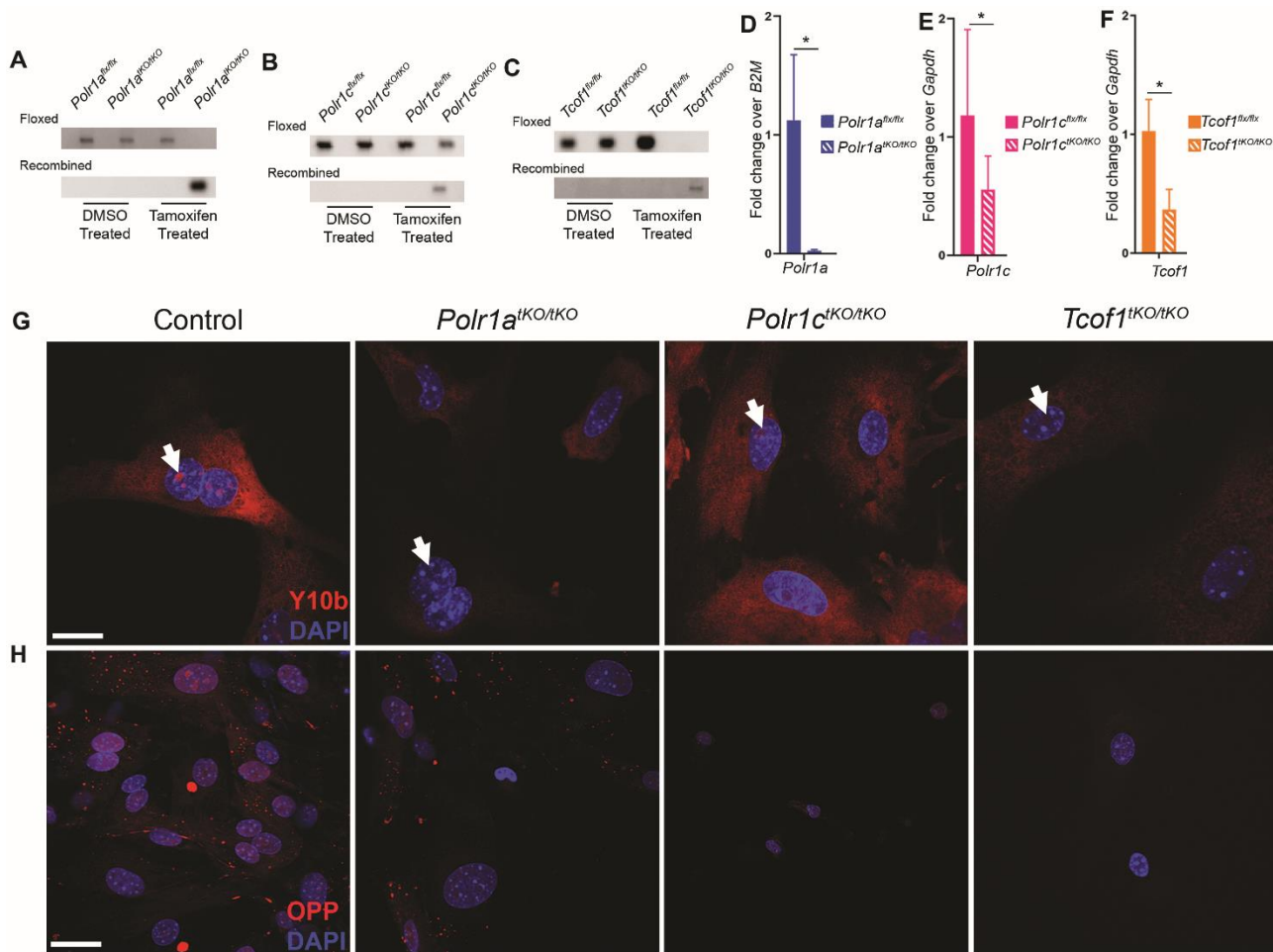**Fig. S12.** *Polr1a*$^{tKO/tKO}$, *Polr1c*$^{tKO/tKO}$ **and** *Tcof1*$^{tKO/tKO}$ **mouse embryonic fibroblast cells have defects in protein synthesis.** (A-C) Recombined DNA is specifically present in tamoxifen treated *Polr1a*$^{tKO/tKO}$, *Polr1c*$^{tKO/tKO}$ and *Tcof1*$^{tKO/tKO}$ MEFs**.** (D-F) Tamoxifen-treated MEFs generated from *Polr1a*$^{tKO/tKO}$, *Polr1c*$^{tKO/tKO}$ and *Tcof1*$^{tKO/tKO}$ mutant embryos have reduced expression of *Polr1a*, *Polr1c* and *Tcof1* transcripts, respectively. * indicates p<0.05, Student's t-test. (G) Tamoxifen-treated *Polr1a*$^{tKO/tKO}$, *Polr1c*$^{tKO/tKO}$ and *Tcof1*$^{tKO/tKO}$ MEFs have reduced expression of Y10b (red) that labels 5.8S rRNA. Staining within the nucleolus is diminished in tKO MEFs relative to controls (white arrowheads). Scale bar = 50 μm (H) New protein synthesis is significantly reduced in *Polr1a*$^{tKO/tKO}$, *Polr1c*$^{tKO/tKO}$ and *Tcof1*$^{tKO/tKO}$ as observed by OPP staining (red). Scale bar = 140 μm.
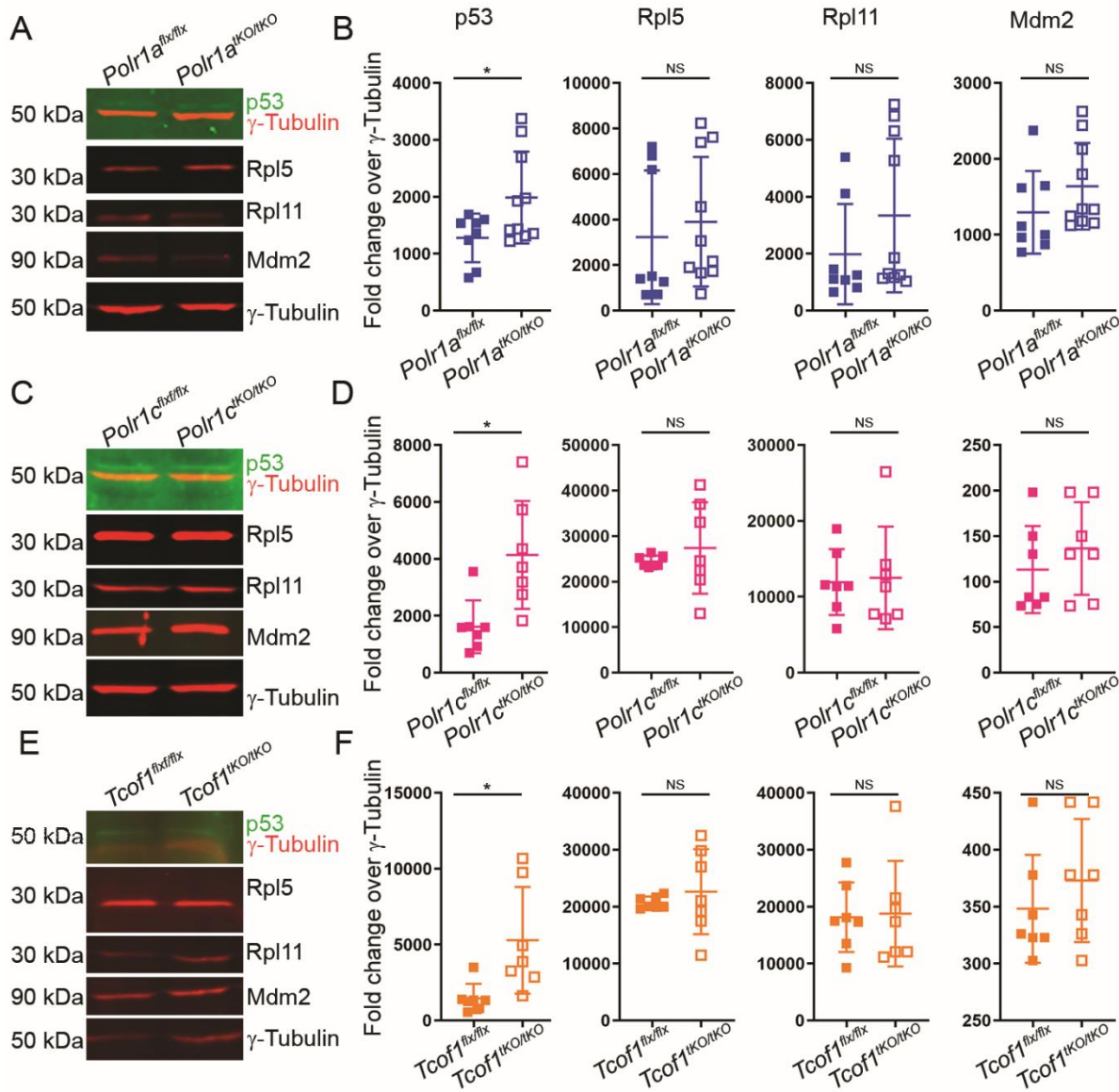
Fig. S13. p53 upregulation is observed in *Polr1a^{tKO/tKO}*, *Polr1c^{tKO/tKO}* and *Tcof1^{tKO/tKO}* mouse embryonic fibroblast cells. Western blot analysis (A, C, E) demonstrates increased p53 expression/accumulation in *Polr1a^{tKO/tKO}*, *Polr1c^{tKO/tKO}* and *Tcof1^{tKO/tKO}* MEFs (quantification in B, D, F). In contrast, the levels of Rpl5, Rpl11 and Mdm2 levels are not significantly changed between controls and *Polr1a^{tKO/tKO}*, *Polr1c^{tKO/tKO}* and *Tcof1^{tKO/tKO}* MEFs. γ-Tubulin was used as a loading control and fold change was calculated as a ratio of band intensities. * indicates p<0.05, Student's t-test. Abbreviations: NS, not significant.
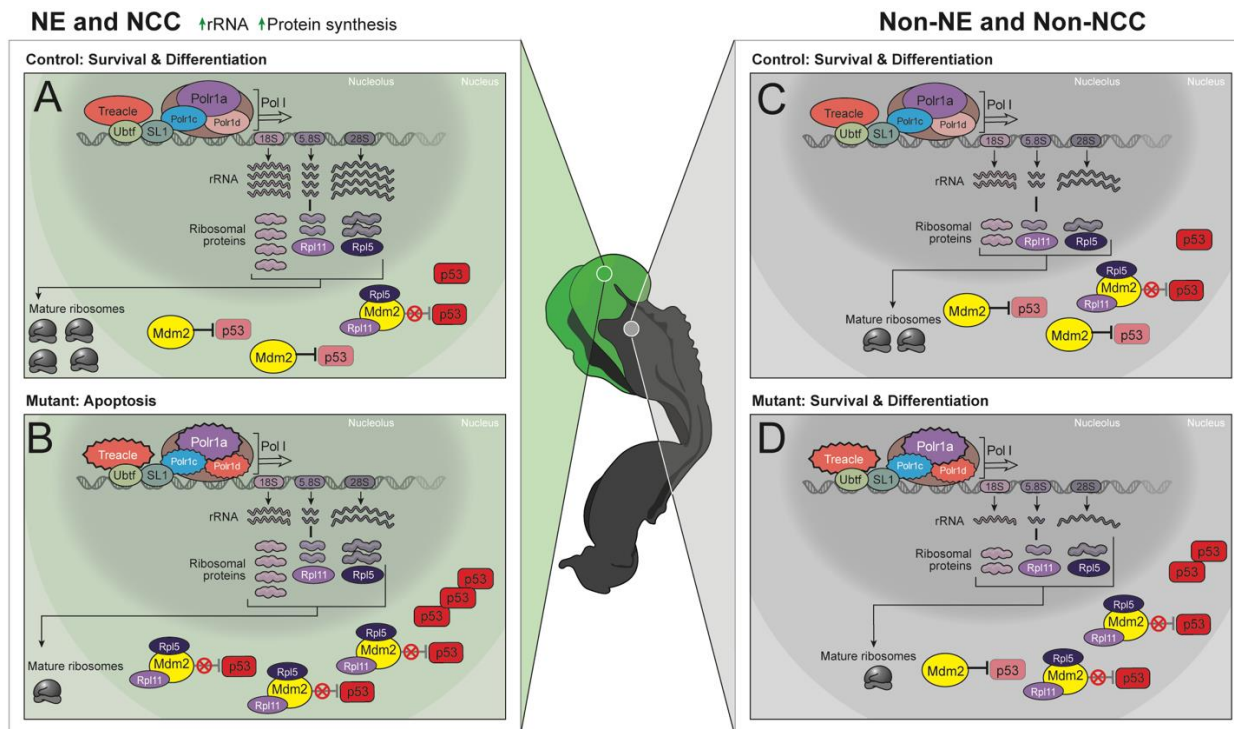
Fig. S14. NCC are more sensitive to disruptions in rRNA transcription, which leads to increased susceptibility to p53-dependent cell death. (A) rRNA and ribosomal proteins are maintained in balanced quantities for proper ribosome assembly. The neuroepithelium (NE) and NCC are highly proliferative and have elevated levels of rDNA transcription relative to surrounding tissues, and thus high levels of ribosomal proteins. During normal cell growth and proliferation, Mdm2 protein binds to, and ubiquitinates p53, targeting it for degradation. This typically keeps p53 at low levels and maintains cell survival. (B) Increased levels of rDNA transcription make NE and NCC highly susceptible to disruptions in Pol I mediated transcription. Disruption of rRNA synthesis due to deletion in Pol I subunits Polr1a, Polr1c, Polr1d, or associated factor Treacle, results in increased free ribosomal proteins and thus binding of Rpl5 and Rpl11 to Mdm2. This inhibits Mdm2 binding and degradation of p53 resulting in p53 protein accumulation. Increased p53 results in NCC apoptosis and craniofacial malformations. (C) Cells with lower proliferative capacity than NE and NCC, have lower rDNA transcription, less rRNA and ribosomal proteins. (D) Upon disruption of rRNA synthesis in these cells, the levels of free ribosomal proteins remain low with little binding of Rpl5 and Rpl11 to Mdm2. Thus, Mdm2 continues to bind to and ubiquitinate p53 targeting it for degradation, which helps to keep p53 protein levels low in support of cell survival.
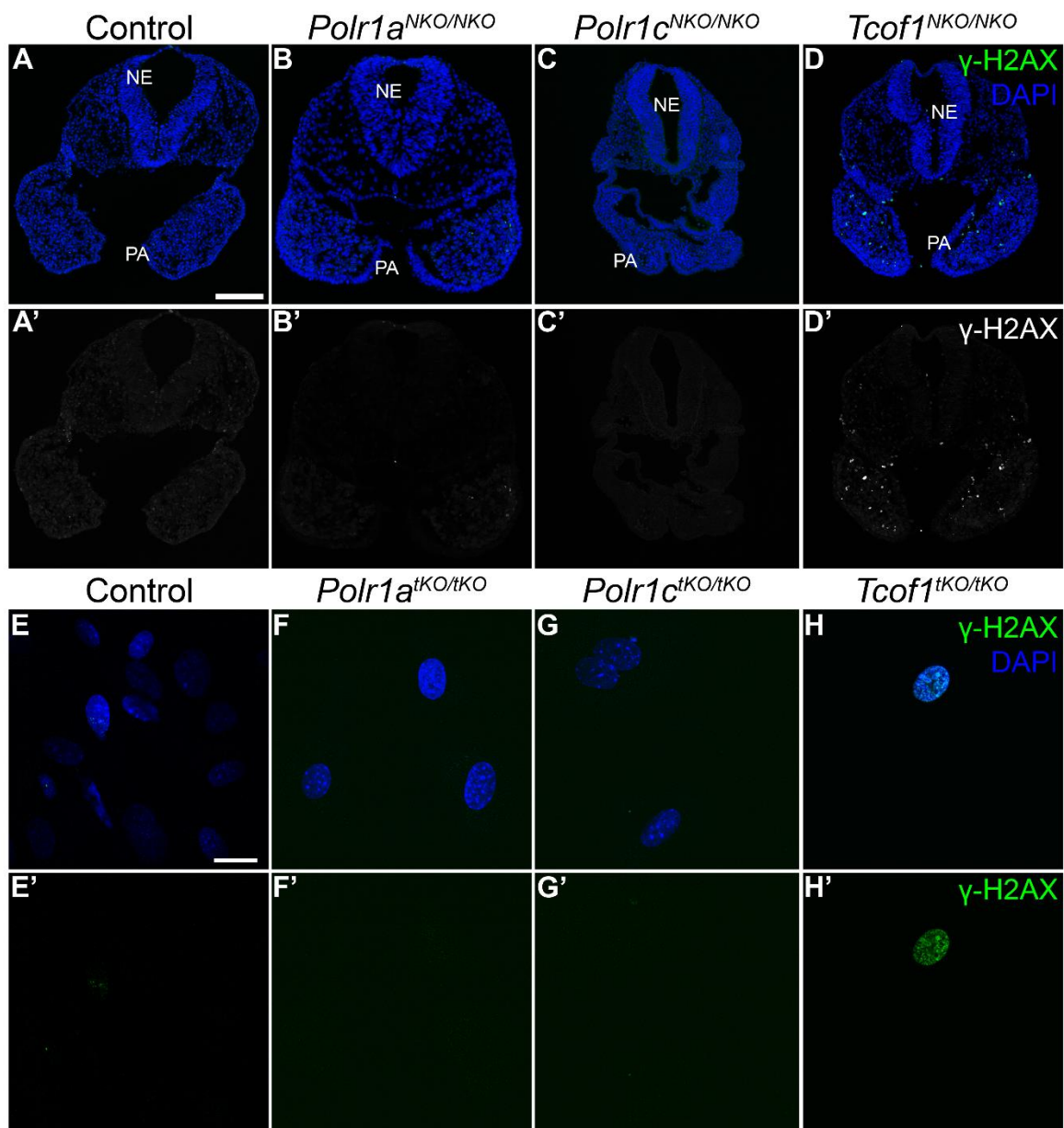
**Fig. S15. DNA damage in *Polr1a^NKO/NKO^*, *Polr1c^NKO/NKO^* and *Tcof1^NKO/NKO^* mice and *Polr1a^tKO/tKO^*, *Polr1c^tKO/tKO^* and *Tcof1^tKO/tKO^* mouse embryonic fibroblast cells.** (A-D) γ-H2AX staining in transverse sections of E9.5 embryos (green in A-D, white in A'-D') demonstrates minimal DNA damage in the pharyngeal arches of *Polr1a^NKO/NKO^* and *Polr1c^NKO/NKO^*, compared to the *Tcof1^NKO/NKO^* mice. Abbreviations. NE, neuroepithelium; PA, pharyngeal arches; Scale bar = 100 μm. (E-H) γ-H2AX staining (green) indicates that *Polr1a^tKO/tKO^* and *Polr1c^tKO/tKO^* MEFs do not undergo DNA damage (F, G), while *Tcof1^tKO/tKO^* MEFs have high expression of γ-H2AX in the nucleus (H). Scale bar = 50 μm.

Table S1. Top 30 proteins identified by multidimensional protein identification technology with Tcof1/Treacle as the bait on 293-FRT cells.

NCBI_Gene	Tcof1 dNSAF AVG	Tcof1 Detected # Out of 7	Control dNSAF AVG	Control Detected # Out of 3	Tcof1/Control:QSPEC:LogFoldChange	Tcof1/Control:QSPEC:Zstatistic	Tcof1/Control:QSPEC:fdr	Tcof1/Control: QSPEC:FDRup	Description	Locus
TCOF1	0.001223	7	0.000036	1	3.298	9.0318	0	0	treacle protein isoform d [Homo sapiens]	NP_001128715.1
TCOF1	0.001165	7	0.000037	1	3.736	6.0336	0	0	treacle protein isoform e [Homo sapiens]	NP_001128716.1
TCOF1	0.001098	7	0.000037	1	3.439	9.2526	0	0	treacle protein isoform g [Homo sapiens]	NP_001182070.1
TCOF1	0.001288	7	0.000036	1	3.501	5.1404	0.000023	0.000002	treacle protein isoform h [Homo sapiens]	NP_001358552.1
RAD50	0.001896	6	0.000041	1	4.526	8.7258	0	0	DNA repair protein RAD50 [Homo sapiens]	NP_005723.2
POLR1A	0.003174	6	0.000062	1	4.15	13.403	0	0	DNA-directed RNA polymerase I subunit RPA1 [Homo sapiens]	NP_056240.2
ARHGAP10	0.003445	5	0	0	3.686	6.3699	0	0	rho GTPase-activating protein 10 [Homo sapiens]	NP_078881.3
POLR1B	0.001749	5	0	0	3.585	5.2961	0.00001	0.000001	POLR1B. NP_001269701.1:DNA-directed RNA polymerase I subunit RPA2 isoform 3 [Homo sapiens] ;NP_001358898.1:DNA-directed RNA polymerase I subunit RPA2 isoform 7 [Homo sapiens] ;NP_061887.2:DNA-directed RNA polymerase I subunit RPA2 isoform 1 [Homo sapiens] ;	NP_001269701.1
CSNK2A1	0.005889	6	0.000109	2	3.496	6.576	0	0	casein kinase II subunit alpha isoform a [Homo sapiens]	NP_808227.1
DHRS2	0.004811	6	0	0	3.405	4.2679	0.001514	0.000155	DHRS2.NP_005785.1:dehydrogenase/reductase SDR family member 2, mitochondrial isoform 2 [Homo sapiens] ;NP_878912.1:dehydrogenase/reductase SDR family member 2, mitochondrial isoform 1 [Homo sapiens] ;	NP_005785.1
POLR1G	0.00338	5	0	0	3.36	6.7439	0	0	POLR1G.NP_001284519.1:DNA-directed RNA polymerase I subunit RPA34 isoform 1 [Homo sapiens] ;NP_036231.1:DNA-directed RNA polymerase I subunit RPA34 isoform 2 [Homo sapiens] ;	NP_001284519.1
EIF2S1	0.003607	5	0	0	3.132	4.3458	0.001083	0.000107	eukaryotic translation initiation factor 2 subunit 1 [Homo sapiens]	NP_004085.1
ARRB2	0.003166	5	0	0	3.117	4.6719	0.000246	0.000022	ARRB2.NP_001244259.1:beta-arrestin-2 isoform 5 [Homo sapiens] ;NP_004304.1:beta-arrestin-2 isoform 1 [Homo sapiens] ;	NP_001244259.1
CSNK2A2	0.003369	6	0.000089	1	2.887	5.9011	0	0	casein kinase II subunit alpha' [Homo sapiens]	NP_001887.1
POLR1E	0.002158	7	0.000128	2	2.824	5.6779	0.000001	0	DNA-directed RNA polymerase I subunit RPA49 isoform 1 [Homo sapiens]	NP_071935.1
USP7	0.000736	6	0.000099	1	2.733	4.6283	0.000302	0.000028	USP7. NP_001273386.2:ubiquitin carboxyl-terminal hydrolase 7 isoform 2 [Homo sapiens] ;NP_001273387.1:ubiquitin carboxyl-terminal hydrolase 7 isoform 3 [Homo sapiens] ;NP_001308787.1:ubiquitin carboxyl-terminal hydrolase 7 isoform 4 [Homo sapiens] ;NP_003461.2:ubiquitin carboxyl-terminal hydrolase 7 isoform 1 [Homo sapiens] ;	NP_001273386.2
ELOA	0.000905	5	0	0	2.575	4.4364	0.000727	0.00007	elongin-A [Homo sapiens]	NP_003189.2
CSNK2B	0.004759	7	0.000435	1	2.483	5.2497	0.000013	0.000001	casein kinase II subunit beta isoform 1 [Homo sapiens]	NP_001311.3
EIF2S3	0.002119	5	0.000198	1	2.162	5.2886	0.00001	0.000001	eukaryotic translation initiation factor 2 subunit 3 [Homo sapiens]	NP_001406.1
POLR2E	0.004011	4	0	0	2.135	4.2359	0.001734	0.000178	DNA-directed RNA polymerases I, II, and III subunit RPABC1 isoform a [Homo sapiens]	NP_002686.2
SRP14	0.010629	5	0.001375	1	2.085	7.0669	0	0	signal recognition particle 14 kDa protein isoform 1 [Homo sapiens]	NP_003125.3
PARP1	0.002039	7	0.000167	3	2.081	6.5056	0	0	poly [ADP-ribose] polymerase 1 [Homo sapiens]	NP_001609.2
POLR1C	0.002206	7	0	0	3.112	3.5546	0.024123	0.002989	DNA-directed RNA polymerases I and III subunit RPAC1 isoform 1 [Homo sapiens]	NP_976035.1
RAB11FIP5	0.000534	5	0	0	2.581	3.9516	0.005492	0.000615	rab11 family-interacting protein 5 isoform 1 [Homo sapiens]	NP_001358201.1
MTDH	0.001025	5	0	0	2.491	3.847	0.008221	0.000958	MTDH.NP_001350066.1:protein LYRIC isoform 3 [Homo sapiens] ;NP_001350067.1:protein LYRIC isoform 4 [Homo sapiens] ;NP_848927.2:protein LYRIC isoform 1 [Homo sapiens] ;	NP_001350066.1
SYNE2	0.000116	3	0	0	2.391	3.9712	0.005086	0.000569	SYNE2.NP_055995.4:nesprin-2 isoform 1 [Homo sapiens] ;NP_878918.2:nesprin-2 isoform 5 [Homo sapiens] ;	NP_055995.4
EIF2S2	0.001543	6	0	0	2.377	3.5662	0.023148	0.002888	EIF2S2.NP_001303293.1:eukaryotic translation initiation factor 2 subunit 2 isoform 3 [Homo sapiens] ;NP_003899.2:eukaryotic translation initiation factor 2 subunit 2 isoform 1 [Homo sapiens] ;	NP_001303293.1
PRPS2	0.002832	3	0.000218	1	2.291	3.6977	0.014376	0.001722	ribose-phosphate pyrophosphokinase 2 isoform 1 [Homo sapiens]	NP_001034180.1

RAB11FIP2	0.000804	5	0	0	**2.097**	**3.5342**	0.025933	0.003239	rab11 family-interacting protein 2 isoform 1 [Homo sapiens]	NP_055719.1
MRE11	0.001144	7	0.000075	1	**3.17**	**3.2533**	0.067188	0.008887	MRE11.NP_001317276.1:double-strand break repair protein MRE11 isoform 3 [Homo sapiens] ;NP_005581.2:double-strand break repair protein MRE11 isoform 2 [Homo sapiens] ;NP_005582.1:double-strand break repair protein MRE11 isoform 1 [Homo sapiens] ;	NP_001317276.1
RPS15A	0.006137	4	0.00048	1	**2.074**	**3.4291**	0.037405	0.004749	40S ribosomal protein S15a [Homo sapiens]	NP_001025180.1
SRP9	0.004466	5	0	0	**2.072**	**3.1228**	0.101045	0.013842	signal recognition particle 9 kDa protein isoform 2 [Homo sapiens]	NP_003124.1
NBN	0.000844	5	0	0	**2.766**	**2.9583**	0.162501	0.023516	nibrin isoform 1 [Homo sapiens]	NP_002476.2

_dNSAF   Distributed Normalized Spectral Abundance Factor

Table S2. List of primers used for genotyping and qRT-PCR.

	Forward	Reverse
Polr1a-WT	GATGCAGTTGGCAATTTCAAGACC	CGGTGTGCTTTCTGCTTCATGC
Polr1a-PostFlp	GATGCAGTTGGCAATTTCAAGACC	CGGTGTGCTTTCTGCTTCATGC
Polr1a-floxed	GAGATGGCGCAACGCAATTAATG	GACCCAAATGTGGAGCATAAGACACC
Polr1a-Cre-excised	GATGCAGTTGGCAATTTCAAGACC	GACCCAAATGTGGAGCATAAGACACC
5'ETS	CAGAATGCCCTTGGAAGA	ACACAGGGAAACCAGAAG
28S	GGGTGGTAAACTCCATCTAA	CCCTCTTGAACTCTCTCTTC
Gapdh	TGGCCAAGGTCATCCATGA	CAGTCTTCTGGGTGGCAGTGA
B2m	CACTGACCGGCCTGTATGC	GGTGGCGTGAGTATACTTGAATTTG
Canx	CCAGACCCTGATGCAGAGAAG	CCTCCCATTCTCCGTCCATA
Polr1a-exon1	CCGAAGAGCTCAAGAAGTTA	GACCCAAAGCCAAATCATAC
p53	TCTCCGAAGACTGGATGA	CTGGAGGAAGTAGTTTCCATAA
Tcof1-exon1	CGTGCACGTGAATCCCCT	CCGCTCTGCTCCTTTACTTCC
Polr1c-exon3	TATGATGATGCCTGGGAC	TCGGCACCTCAGCTAACA
p21	GACAAGAGGCCCAGTACTTC	GCTTGGAGTGATAGAAATCTGTC

References

1. Skarnes WC*, et al.* (2011) A conditional knockout resource for the genome-wide study of mouse gene function. *Nature* 474(7351):337-342.
2. Kranz A*, et al.* (2010) An improved Flp deleter mouse in C57Bl/6 based on Flpo recombinase. *Genesis (New York, N.Y. : 2000)* 48(8):512-520-512—520.
3. Dixon J, Fässler R, & Dixon MJ (2000) Increased levels of apoptosis in the prefusion neural folds underlie the craniofacial disorder, Treacher Collins syndrome. in *Human Molecular Genetics*, pp 1473-1480.
4. Aoto K*, et al.* (2015) Mef2c-F10N enhancer driven β-galactosidase (LacZ) and Cre recombinase mice facilitate analyses of gene function and lineage fate in neural crest cells. *Dev Biol* 402(1):3-16.
5. Jiang X, Rowitch DH, Soriano P, McMahon AP, & Sucov HM (2000) Fate of the mammalian cardiac neural crest. *Development* 127(8):1607-1607.
6. Chai Y*, et al.* (2000) Fate of the mammalian cranial neural crest during tooth and mandibular morphogenesis. *Development* 127(8):1671-1671.
7. Sakai D, Dixon J, Achilleos A, Dixon M, & Trainor PA (2016) Prevention of Treacher Collins syndrome craniofacial anomalies in mouse models via maternal antioxidant supplementation. *Nature Communications* 7(1):10328.
8. Florens L & Washburn MP (2006) Proteomic analysis by multidimensional protein identification technology. *Methods Mol Biol* 328:159-175.
9. Washburn MP, Wolters D, & Yates JR (2001) Large-scale analysis of the yeast proteome by multidimensional protein identification technology. *Nature Biotechnology* 19(3):242-247.
10. Dennis JF*, et al.* (2012) Mutations in Hedgehog acyltransferase (Hhat) perturb Hedgehog signaling, resulting in severe acrania-holoprosencephaly-agnathia craniofacial defects. *PLoS genetics* 8(10):e1002927-e1002927.
11. Munoz W & Trainor P (2019) Mouse Embryo Culture for the Study of Neural Crest Cells. *Methods in molecular biology (Clifton, N.J.)*), Vol 1976, pp 107-119.
12. Behringer R, Gertsenstein M, Nagy V, & Nagy A (2014) *Manipulating the Mouse Embryo: A Laboratory Manual, Fourth Edition* 4 Ed.
13. Schindelin J*, et al.* (2012) Fiji: an open-source platform for biological-image analysis. *Nature methods* 9(7):676-682.
14. Xu J (2005) Preparation, Culture, and Immortalization of Mouse Embryonic Fibroblasts. *Current Protocols in Molecular Biology* 70(1):28.21.21-28.21.28.
15. Dash S, Bhatt S, Falcon KT, Sandell LL, & Trainor PA (2020) Med23 Regulates Sox9 Expression during Craniofacial Development. *Journal of Dental Research*:0022034520969109-0022034520969109.
16. Echelard Y, Vassileva G, & McMahon AP (1994) Cis-acting regulatory sequences governing Wnt-1 expression in the developing mouse CNS. *Development* 120(8):2213-2213.
17. Brault V*, et al.* (2001) Inactivation of the (β)-catenin gene by Wnt1-Cre-mediated deletion results in dramatic brain malformation and failure of craniofacial development. *Development* 128(8):1253-1253.
18. Satija R, Farrell JA, Gennert D, Schier AF, & Regev A (2015) Spatial reconstruction of single-cell gene expression data. *Nature Biotechnology* 33(5):495-502.
19. Hafemeister C & Satija R (2019) Normalization and variance stabilization of single-cell RNA-seq data using regularized negative binomial regression. *Genome Biology* 20(1):296-296.